

# 1 **ECOMAN: an open-source package for geodynamic and** 2 **seismological modelling of mechanical anisotropy.**

3 Manuele Faccenda<sup>1\*</sup>, Brandon P. VanderBeek<sup>1\*</sup>, Albert de Montserrat<sup>2</sup>, Jianfeng Yang<sup>3</sup>, Francesco  
4 Rappisi<sup>4</sup>, Neil Ribe<sup>5</sup>

5 <sup>1</sup>Dipartimento di Geoscienze, Università di Padova, 35131, Padova, Italy.

6 <sup>2</sup>Institute of Geophysics, ETH Zürich, Sonneggstrasse 5, 8092, Zürich, Switzerland.

7 <sup>3</sup>State Key Laboratory of Lithospheric Evolution, Institute of Geology and Geophysics, Chinese Academy of Sciences, Beijing,  
8 China.

9 <sup>4</sup>School of Earth and Environment, University of Leeds.

10 <sup>5</sup>Lab FAST, Univ Paris-Saclay, CNRS, Bat 530, rue André Rivière, F-91405 Orsay, France.

11

12 *Correspondence to:* Manuele Faccenda ([manuele.faccenda@unipd.it](mailto:manuele.faccenda@unipd.it)), Brandon P. Vanderbeek  
13 ([brandonpaul.vanderbeek@unipd.it](mailto:brandonpaul.vanderbeek@unipd.it))

14 **Abstract.** Mechanical anisotropy related to rock fabrics is a proxy for constraining the Earth's deformation patterns. However,  
15 the forward and inverse modelling of mechanical anisotropy in 3D large-scale domains has been traditionally hampered by the  
16 intensive computational cost and the lack of a dedicated, open-source computational framework. Here we introduce ECOMAN,  
17 a software package for modelling strain-/stress-induced rock fabrics and testing the effects of the resulting elastic and viscous  
18 anisotropy on seismic imaging and mantle convection patterns.

19 Differently from existing analogous software, ECOMAN can model strain-induced fabrics across all mantle levels and is  
20 optimised to run efficiently on multiple CPUs. It also enables modelling of shape preferred orientation (SPO)-related structures  
21 that can be superimposed over lattice/crystallographic preferred orientation (LPO/CPO) fabrics, which allows the consideration  
22 of the mechanical effects of fluid-filled cracks, foliated/lineated grain-scale fabrics and rock-scale layering.

23 One of the most important innovations is the Platform for Seismic Imaging (PSI), a set of programs for performing forward  
24 and inverse seismic modelling in isotropic/anisotropic media using real or synthetic seismic datasets. The anisotropic inversion  
25 strategy is capable of recovering parameters describing a tilted transversely isotropic (TTI) medium, which is required to  
26 reconstruct 3D structures and mantle strain patterns and to validate geodynamic models.

## 27 **1 Introduction**

28 The study of the Earth's interior has been traditionally based on seismological and geodynamic modelling, the former providing  
29 important information about its present-day structure, composition and state (Chang et al., 2015; French and Romanowicz,  
30 2015; Schaeffer et al., 2016; Debayle et al., 2020), and the latter about its dynamics and compositional evolution (Davies et

31 al., 2012; Cramer and Tackley, 2014; Müller et al., 2022). Seismological and geodynamical modelling are very often  
32 conducted independently, which creates mechanical and geometrical inconsistencies across the models, hampers the  
33 interpretation of seismic observations in terms of geodynamic processes, and exacerbates the non-uniqueness of geodynamic  
34 model predictions. An alternative approach is combining computational seismology and geodynamics with mineral physics,  
35 which provides a comprehensive understanding of the Earth's interior processes, seismic behaviour, and material properties.  
36 This multidisciplinary methodology has been used in previous studies to post-process geodynamic flow calculations with  
37 thermodynamically self-consistent models of mantle mineralogy and converting thermal structure into isotropic elastic  
38 parameters. The obtained seismic mantle structure can then be used in simulations of global wave propagation, such that  
39 specific hypotheses on mantle dynamics can be tested directly against seismic data (Styles et al., 2011; Schubert et al., 2012;  
40 Maguire et al., 2018). The inverse procedure consists of converting seismic anomalies into density anomalies driving mantle  
41 flow models and is typically employed to quantify dynamic topography and mantle viscosity structure, and to reproduce large-  
42 scale mantle flow patterns (e.g., Bunge et al., 2003; Steinberger and Calderwood, 2006; Rudolph et al., 2015). However,  
43 isotropic seismic imaging provides limited information regarding local-/regional-scale dynamical processes (Fraters and  
44 Billen, 2021), and a better way to couple the geodynamic evolution and seismological structure of the Earth's interior is by  
45 accounting for the strain-/stress-induced mechanical anisotropy of crustal and mantle rocks.

46 Mechanical anisotropy refers to the directional dependence of mechanical properties in a material and is well known to affect  
47 both elastic and viscous deformational behaviour. Mechanical anisotropy depends on several factors, including the lattice or  
48 crystal preferred orientation (LPO, CPO) of intrinsically anisotropic minerals, and extrinsic mechanisms related to the shape  
49 preferential orientation (SPO) of melt, fluid, or air-filled fractures and non-spherical pores, and grain- or rock-scale  
50 compositional layering. Most micro- and macro-scale fabrics are acquired as a function of the cumulative deformation and  
51 material mechanical properties, and as such they constitute an important source of information about the Earth's dynamical  
52 behaviour.

53 Elastic anisotropy is directly connected to seismic anisotropy, which is a phenomenon in which the seismic wave speed varies  
54 as a function of the propagation direction. It is mainly observed in the crust, mantle boundary layers, and inner core (Almqvist  
55 and Mainprice, 2017; Karato, 1998; Kendall, 2000; Long and Becker, 2010; Deuss, 2014). Understanding and modelling  
56 seismic anisotropy is crucial for determining long-term deformational patterns and the present-day stress field in the crust, and  
57 constraining geodynamic modelling predictions (Jadamec and Billen, 2010; Hu et al., 2017; Zhou et al., 2018; Lo Bue et al.,  
58 2022). In addition, the ability to account for anisotropic effects can improve the quality of subsurface imaging. Indeed, it has  
59 been demonstrated that, because of the uneven seismic ray coverage, failing to account for seismic anisotropy may generate  
60 strong artefacts that substantially bias our understanding of mantle structures and dynamics in different tectonic settings  
61 (Bezada et al., 2016; VanderBeek and Faccenda, 2021; VanderBeek et al., 2023; Faccenda and VanderBeek, 2023).  
62 Considering the widespread presence of seismic anisotropy, anisotropic seismic models provide a more realistic representation  
63 of the Earth's subsurface compared to isotropic models.

64 Viscous anisotropy modelling refers to the study and simulation of materials that exhibit varying degrees of viscosity  
65 (resistance to viscous deformation) in different directions. Although viscous anisotropy has been traditionally associated with  
66 the mechanical behaviour of multi-layered media (Mühlhaus et al., 2002; Kocher et al., 2006), it has been also observed in  
67 experimentally-deformed mica-rich and olivine crystal aggregates (Shead and Kronenberg, 1993; Hansen et al., 2012).  
68 Previous numerical studies demonstrated that viscous anisotropy can potentially stabilise long-wavelength convective patterns  
69 (Christensen, 1987; Mühlhaus et al., 2004) and more generally affect processes such as plate motion (Kiraly et al., 2020), post-  
70 glacial rebound (Han and Wahr, 1997), lithospheric shear zone reactivation (Tommasi et al., 2009) and dripping (Lev and  
71 Hager, 2008).

72 Over the last few years a few attempts have been made to integrate micro-mechanical modelling of fabric evolution with large-  
73 scale geodynamic models using either directors (Lev et al., 2008; Halter et al., 2022), the CPO model D-REX (Kaminski et  
74 al., 2004; Becker et al., 2006; Jadamec and Billen, 2010; Faccenda and Capitanio, 2013; Faccenda, 2014; Ito et al., 2014; Hu  
75 et al., 2017; Zhou et al., 2018; Fraters and Billen, 2021), or the CPO model Visco-Plastic Self Consistent (VPSC; Tommasi et  
76 al., 2009; Li et al., 2014). However, each of these methodologies has its own limitations mainly associated with either the  
77 accuracy of the estimates, the large computational burden or software accessibility, which have impeded a more widespread  
78 diffusion in the geodynamic community. At the same time, the recovery of 3D seismic anisotropy patterns has been  
79 traditionally considered intractable due to the highly underdetermined nature of the inverse problem, and, although it has been  
80 addressed by several previous studies (e.g., Debayle et al., 2005; Panning et al., 2006; Abt and Fischer, 2008; Long et al.,  
81 2008; Wookey, 2012; Mondal and Long, 2019), only recently a theoretical background and computational algorithms have  
82 been developed to simultaneously invert for P- and/or S-wave isotropic velocity anomalies and anisotropy resulting from  
83 arbitrarily oriented structures ( Munzarova et al., 2018; VanderBeek and Faccenda, 2021; Rappisi et al., 2022; Wang and Zhao,  
84 2022; VanderBeek et al., 2023; Del Piccolo et al., 2023). Yet, to date there is no freely-available software capable of modelling  
85 seismic anisotropy related to arbitrarily oriented structures.

86 In this contribution we present the new and open-source software package ECOMAN (**E**xploring the **C**onsequences of  
87 **M**echanical **A**nisotropy) that enables linking seismology and geodynamics by providing a set of computationally optimised  
88 programs for (i) estimating rock mechanical anisotropy as a function of the geodynamic model deformation history, and  
89 compositional, rheological, stress, pressure, temperature, fields, and (ii) solving forward/inverse seismological problems  
90 accounting for seismic anisotropy. In the next sections, we first describe the different ECOMAN modules, after which we  
91 discuss the advantages and limitations of the software package, and the roadmap for future developments.

92

93 Table 1. Abbreviations and their description. Units are indicated for dimensional physical properties.

Abbreviation	Description	

UM	Upper mantle	
UTZ	Upper mantle transition zone	
LTZ	Lower mantle transition zone	
LM	Lower mantle	
LPO/CPO	Lattice/crystal preferred orientation	
SPO	Shape preferred orientation	
FSE	Finite Strain Ellipsoid, defined by the eigenvalues and eigenvectors of <b>LS</b>	
STILWE	Smoothed Transversely Isotropic Long-Wavelength Equivalent	
DEM	Differential Effective Medium	
VPSC	Visco-Plastic Self Consistent	
MDM	Modified Director Method	
		Units
$\rho$	Density	kg/m <sup>3</sup>
P	Pressure	Pa
T	Temperature	K
Fd	Fraction of dislocation creep deformation	-
<b>V</b> , $V_i$	Velocity vector and its components	m/s
<b>F</b> , $F_{ij}$	2 <sup>nd</sup> -order deformation gradient tensor and its components	-
<b>LS</b> , $LS_{ij}$	2 <sup>nd</sup> -order left stretch tensor and its components	-
<b>C</b> , $C_{\alpha\beta}$	4 <sup>th</sup> -order elastic tensor and its components in Voigt notation	GPa
<b>S</b> , $S_{\alpha\beta}$	4 <sup>th</sup> -order compliance tensor and its components in Voigt notation	GPa <sup>-1</sup>
<b><math>\eta</math></b> , $\eta_{\alpha\beta}$	4 <sup>th</sup> -order normalised viscous tensor and its components in Voigt notation	-

## 95 **2 Software package structure**

96 ECOMAN includes several programs that are complementary and can be grouped into three main categories (Fig. 1):

97

98 1) programs that estimate strain/stress-induced rock fabrics (LPO and SPO) and their elastic and viscous anisotropic  
99 mechanical properties (D-REX\_S, D-REX\_M, EXEV);

100 2) programs that post-process the simulated rock fabrics for visualisation of their isotropic/anisotropic mechanical  
101 properties and deformational history (VIZTOMO, VIZVISC), and format the elastic tensors generating input files for  
102 seismological synthetics (VIZTOMO);

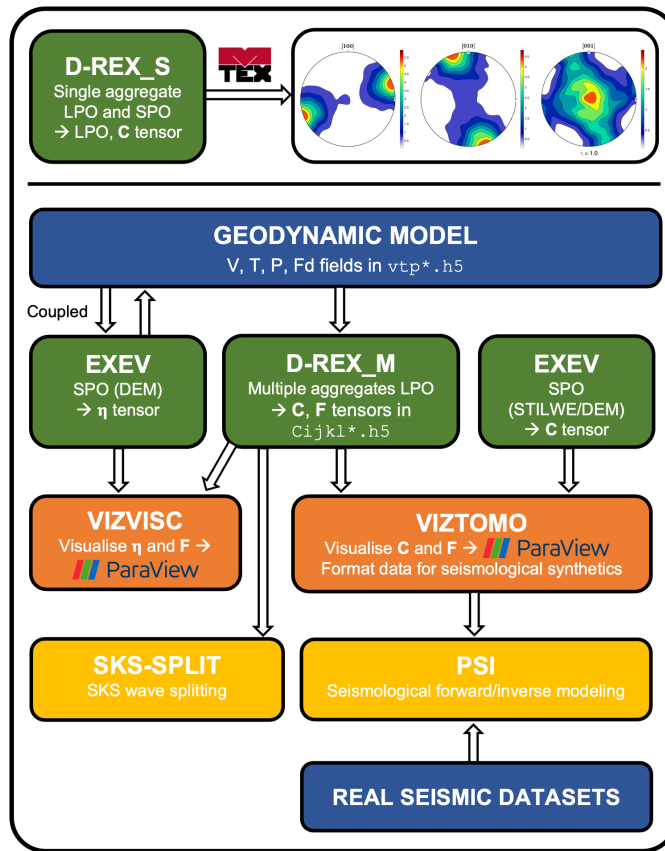
103 3) programs that test the elastic response of anisotropic media by performing seismological forward/inverse modelling  
104 and, in particular, isotropic and anisotropic seismic tomographies on synthetic and real seismic datasets (SKS-SPLIT,  
105 PSI).

106

107 Most of the code modules are written in the Fortran programming language, except for the PSI program that is written in Julia.

108 Visualisation of the output is done through the MATLAB MTEX toolbox (Mainprice et al., 2011) for single aggregate fabrics,  
109 and ParaView (Ahrens et al., 2005) for 2D and 3D simulations.

110



111

112 **Figure 1.** ECOMAN structure and flow chart. Coloured boxes denote programs that compute rock fabrics (green), post-process the elastic  
 113 (C), viscous ( $\eta$ ) and deformation gradient (F) tensors for visualisation and/or data formatting for seismological synthetics (orange), and  
 114 perform seismological forward/inverse modelling on synthetic or real datasets (yellow). Input data are from geodynamic modelling or real  
 115 seismic datasets (blue). Visualisation of the mechanical properties and LPO can be done with the MTEX MATLAB toolbox for single crystal  
 116 aggregates or the software ParaView for large-scale simulations.

117

## 118 2.1 Rock fabrics and mechanical properties simulations

119 The evolution of the strain-induced LPO can be simulated with the D-REX model (Kaminski et al., 2004), which has been  
 120 adapted to reproduce the fabric evolution of a single (D-REX\_S) or multiple (D-REX\_M) two-mineral phase aggregates  
 121 representative of the entire Earth's mantle. The accuracy of the D-REX model has been tested against analytical solutions  
 122 derived by Fraters and Billen (2021) (Appendix A). Five sets of two-mineral phases mantle aggregates can be defined as a  
 123 function of depth or density  $\rho$  (Fig. 2; see Table 1 for a list of abbreviations and physical properties):

124

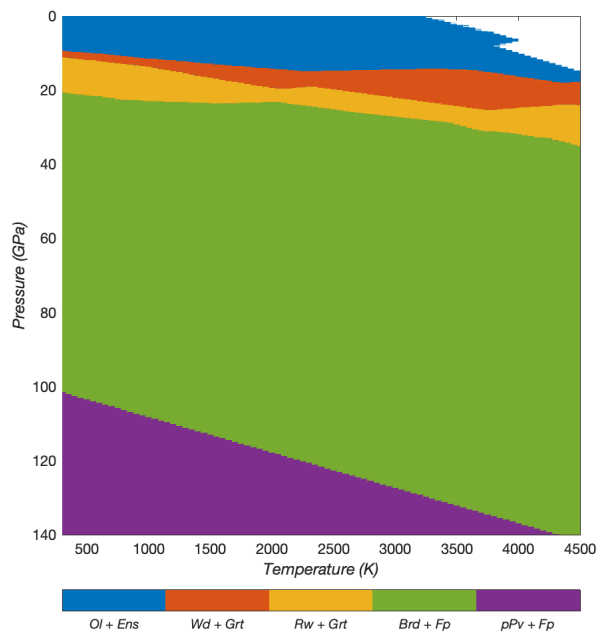
- 125 1) **olivine + enstatite**, for the upper mantle (UM: 0-410 km or  $3000 < \rho \leq 3650$  kg/m<sup>3</sup>);
- 126 2) **wadsleyite + majoritic garnet**, for the upper mantle transition zone (UTZ: 410-520 km or  $3650 < \rho \leq 3870$  kg/m<sup>3</sup>);

- 127 3) ringwoodite + majoritic garnet, for the lower mantle transition zone (LTZ: 520-660 km or  $3870 < \rho \leq 4150 \text{ kg/m}^3$ );
- 128 4) **bridgmanite** + ferropericlae, for the lower mantle (LM: 660-2900 km or  $\rho > 4150 \text{ kg/m}^3$ );
- 129 5) **post-perovskite** + ferropericlae, for the bottom of the lower mantle according to the parametrized phase boundary  
130  $P(\text{GPa}) = 98.7 + T(\text{K}) \cdot 0.00956$  (Oganov and Ono, 2004).

131  
132 The strain-induced LPO is computed for the phases in bold, while other major phases such as garnet, ringwoodite and  
133 ferropericlae are considered to be isotropic and their distribution is set to be random. Thus, no LPO is computed for the LTZ,  
134 such that (minor) anisotropy arises only when SPO modelling due to compositional layering is active (section 2.1.3; Faccenda  
135 et al., 2019). The LPO of wadsleyite, bridgmanite and post-perovskite are computed according to the same D-REX  
136 methodology originally applied to upper mantle phases and described in detail in Kaminski and Ribe (2001), and Kaminski et  
137 al. (2004), but including additional slip systems as indicated in Table A1. For each of these new phases it is possible to define  
138 in the D-REX\_S and D-REX\_M input files the same free parameters of the D-REX model (the dimensionless grain boundary  
139 modility  $M^*$ , nucleation parameter  $\lambda^*$ , threshold volume fraction  $\chi$ , and in addition the power-law exponent for dislocation  
140 creep deformation within the grains) as for upper mantle aggregates. The full elastic tensor is then calculated according to the  
141 crystal orientation, volume fraction, phase abundance, P-T conditions, bulk rock composition, and using Voigt-Reuss-Hill  
142 averaging schemes (see section 2.1.2 and Appendix B for more details).

143 The elastic properties related to strain/stress-induced SPO fabrics can instead be calculated at the grain- or rock-scale and for  
144 layered or two-phase (matrix-ellipsoidal inclusions) systems using the isotropic elastic moduli of the different (fluid, mineral,  
145 rock) components (EXEV).

146 The elastic properties and density of the aggregates characterised by LPO and/or SPO fabrics are estimated at relevant mantle  
147 P-T conditions using the single crystal elastic moduli and their P-T derivatives for the main mineral phases and compiled from  
148 different mineral physics studies, together with lookup tables of the isotropic elastic moduli, density and mineral phase volume  
149 fraction generated with MMA\_EoS (Chust et al., 2017) for five bulk rock compositions (dunite, harzburgite, pyrolite, MORB,  
150 pyroxenite) at temperature and pressure ranges of  $T = 300 : 50 : 4500 \text{ K}$ ,  $P = 0 : 0.1 : 140 \text{ GPa}$ , respectively (see Appendix B  
151 and Tables B1 and B2).



152

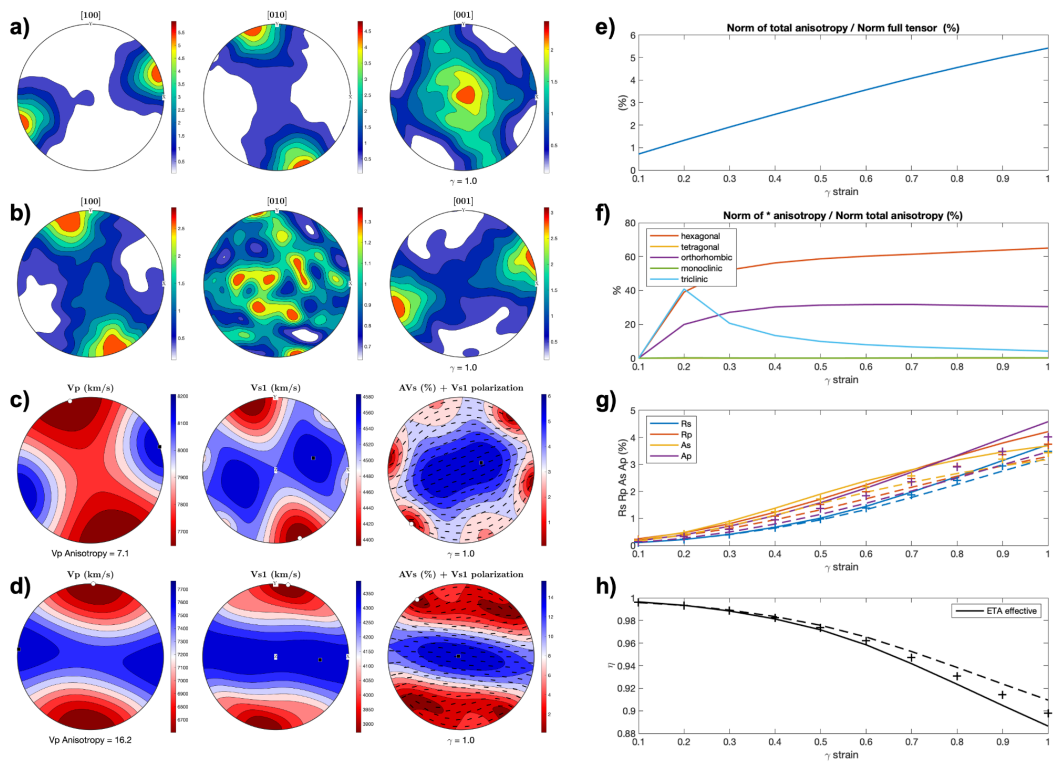
153 **Figure 2.** Two-phase aggregates defined by the density crossovers and Brd-pPv phase transition for a pyrolytic mantle composition.

### 154 2.1.1 D-REX\_S

155 D-REX\_S is a program designed for modelling the evolution of strain-induced LPO fabrics and related elastic properties of a  
 156 single, two-mineral phases mantle aggregate, as a function of the imposed flow field, amount of strain, crystal plasticity, P-T  
 157 conditions and additional effects related to SPO fabrics. It builds on the original D-REX software (Kaminski et al., 2004) for  
 158 modelling the strain-induced LPO, and it includes MATLAB scripts to generate pole figures of the LPO and  
 159 isotropic/anisotropic seismic properties with the MTEX software (Mainprice et al., 2011) (Fig. 3a-d), together with the  
 160 possibility to display the evolving fabric strength (M-index, J-index) and the fraction of different anisotropy components  
 161 (obtained via tensor decomposition; Browaeys et al., 2004; Fig. 3e-h).

162 D-REX\_S is particularly useful for those users who are not familiar with LPO modelling, and more in general, to anyone  
 163 interested in performing parameter sensitivity tests on different mantle mineral aggregates before launching large-scale  
 164 simulations. In addition, the microstructures generated with D-REX\_S can be used in the D-REX\_M 2D-3D simulations to  
 165 impose pre-existing (e.g., fossil) fabrics on multiple crystal aggregates located within a specific subdomain (see section 2.1.2).  
 166 As an application and with the aim of debunking the common misconception that the D-REX model can only produce too  
 167 strong LPO fabrics, here we show that with a suitable choice of D-REX free parameters it is possible to reproduce both weak  
 168 and strong olivine fabrics as recorded in natural samples (Warren et al., 2008) and high-strain laboratory experiments (Hansen  
 169 et al., 2014; Tasaka et al., 2017) (Fig. 4).





170

171

172

173

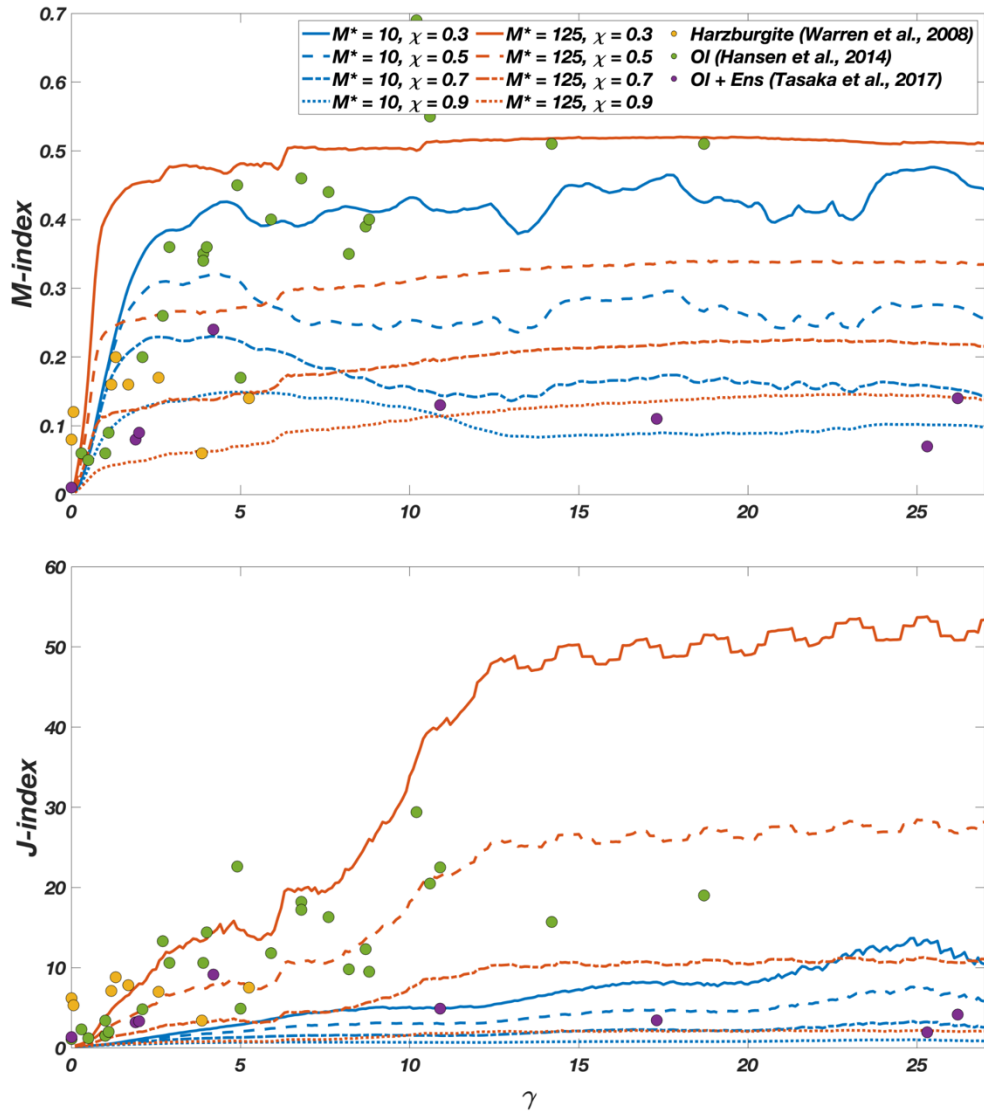
174

175

176

177

**Figure 3.** D-REX\_S output for an upper mantle aggregate (O1:Opx=70:30) subjected to a simple shear deformation of 1. Pole figures of the olivine (a) and orthopyroxene (b) crystallographic axes; (c) pole figures of Vp, Vs1, AVs =  $200(Vs1 - Vs2)/(Vs1 + Vs2)$  with superimposed Vs1 polarisation directions evaluated from the elastic tensor of the two-phase aggregate. (d) same as (c) but with the superimposed effect of an SPO fabric due to 5% melt-filled cracks aligned at -30° from the principal stress (i.e., at 15° from the horizontal plane); (e) fraction of total anisotropy relative to the full elastic tensor and (f) contribution of 5 anisotropic classes relative to the total anisotropy; (g) P- and S-wave radial and azimuthal anisotropy and (h) eta parameter =  $F/(A-2L)$  for the elastic tensors computed with the Voigt (continuous lines), Reuss (dashed lines) and Hill (crosses) averaging schemes, respectively.



178

179

180

181

**Figure 4** –M-index (top) and J-index (bottom) for olivine fabrics developing in simple shear deformation as computed with D-REX\_S using different parameters and compared with data reported in the literature as indicated in the legend. Fixed parameters are  $\lambda^* = 5$ , olivine  $nCRSS = (1, 2, 3, \infty)$ , and the aggregates have a phase abundance of *Ol:Ens* = 70:30 with 1000 crystals for each phase.

182

### 2.1.2 D-REX\_M

183

184

185

186

D-REX\_M is a program that computes the evolution of the LPO and related elastic properties of multiple, two-mineral phases mantle aggregates, as a function of the single crystal plastic and elastic properties, and of the flow field, deformation mechanisms and P-T conditions resulting from 2D-3D geodynamic simulations. It builds on the original D-REX software, which includes routines for estimating the strain-induced LPO and elastic properties (i) for upper mantle polycrystalline

187 aggregates only, (ii) using single crystal elastic tensors derived at room P-T conditions and averaged using a Voigt scheme,  
188 (iii) in a 2D Cartesian domain, (iv) for a single (steady-state) flow field, and (v) whereby the whole deformation is considered  
189 to be accommodated by dislocation creep assisted by grain-boundary sliding (Kaminski et al., 2004). D-REX\_M additionally  
190 models:

- 191 • fabrics relevant to the mid and lowermost mantle (Faccenda, 2014), including those with post-perovskite. Phase  
192 transitions can be set to occur at predefined depths (e.g., 410 km, 660 km). Density crossovers (which allow modelling  
193 the deflection of phase boundaries with a non-zero Clapeyron-slopes; Fig. 7), and parameterized phase boundaries as  
194 for the case of post-perovskite (Oganov and Ono, 2004) are also included;
- 195 • elastic properties and density as a function of the bulk rock composition and local P-T conditions (Faccenda, 2014;  
196 Chang et al., 2016; Ferreira et al., 2019) (Appendix B). The isotropic component of the elastic tensors and density are  
197 taken from the lookup tables generated by MMA-EoS for a given mantle lithology (Table A1), and the anisotropic  
198 component from the mineral single crystal elastic moduli and their pressure and temperature derivatives listed in  
199 Table B2. This strategy ensures a gradual transition of the seismic properties at phase boundaries where phase  
200 transformations occur. Voigt-Reuss-Hill averaging schemes of the elastic moduli are included;
- 201 • non-steady-state flows in 2D/3D Cartesian and polar grids (Faccenda and Capitanio, 2012, 2013, Hu et al., 2017;  
202 Zhou et al., 2018; Lo Bue et al., 2022; Faccenda and VanderBeek, 2023). In polar coordinates the velocity gradient  
203 tensor must be computed in the external Cartesian reference frame, as described in Appendix C. The global-scale  
204 models are spatially discretized using the so-called Yin-Yang grids (Kageyama and Sato, 2004). Several examples  
205 (cookbooks) are provided on how to use the software in different coordinate systems and in steady-state or time-  
206 dependent flow conditions;
- 207 • fabric evolution in the presence of multiple creep mechanisms. At any time step, the fraction of deformation  
208 accommodated by dislocation creep in a given point of the geodynamic model defines the fraction of time spent for  
209 intracrystalline deformation assisted by grain-boundary sliding according to the D-REX model. The remaining time  
210 is used to apply, when present, fluid deformation rotation to the whole crystal aggregate (e.g., Hedjazian et al., 2017)  
211 (Appendix D);
- 212 • a pre-existing (fossil) fabric (pre-computed with D-REX\_S) within a subdomain, typically the lithosphere. This is  
213 often the case for geodynamic models where the lithosphere accretion is not modelled, and its geometry is initially  
214 prescribed.

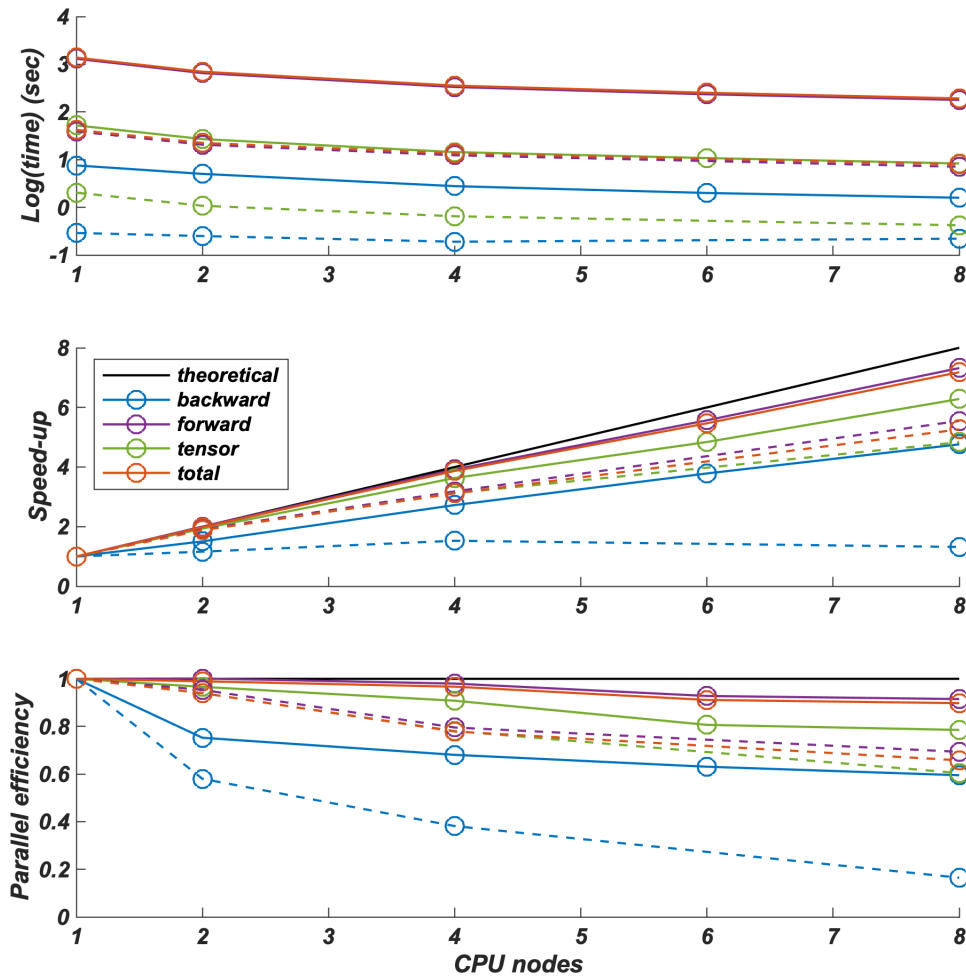
215  
216 The D-REX\_M input files should contain information about the geodynamic model evolution. Critical information are the  
217 components of the velocity vector  $\mathbf{V}$  field, and, for time-dependent flow models, the total elapsed time and timestep. These are  
218 used to compute the velocity gradient tensor, and the LPO evolution and advection of the crystal aggregates. Additional fields  
219 defined on the Cartesian/spherical grid that can be included in the input files are:

- when the geodynamic model is thermo-mechanical, the temperature  $T$  and total pressure  $P$  fields, which can be used to compute the single crystal elastic tensor and aggregate phase transitions as a function of the local  $P$ - $T$  conditions;
- when the rheological model of the geodynamic simulation is based on multiple visco-plastic deformation mechanisms, the fraction of deformation accommodated by dislocation creep  $F_d = \eta_{\text{disl}}/\eta_{\text{eff}}$ , where  $0 \leq F_d \leq 1$ ,  $\eta_{\text{disl}}$  is the viscosity calculated with the dislocation creep flow law,  $\eta_{\text{eff}}$  is the effective viscosity calculated with the harmonic average of each of the viscosities representing a different deformation mechanism.

In summary, the time and the velocity field  $\mathbf{V}$  are essential information, while the  $P$ ,  $T$ ,  $F_d$  fields are optional and depend on the type of (mechanical vs. thermomechanical) geodynamic and (single vs. multiple visco-plastic deformation mechanisms) rheological models.

While the  $\mathbf{V}$ ,  $P$ ,  $T$ ,  $F_d$  fields are defined on the Eulerian grid, the distribution, size, modal composition and mechanical properties of mantle aggregates are defined on the Lagrangian particles. After initialising the Eulerian grid and Lagrangian particles, the entire run consists of three main steps: (i) backward advection of the particles for a given time span or up to a maximum cumulated strain; (ii) forward advection and update of the LPO and deformation gradient tensor  $\mathbf{F}$ ; (iii) computation of the full elastic tensor and creation of the output file. This strategy ensures a homogeneous final distribution of the aggregates (coincident with the initial one) which is desired for visualization of the aggregates mechanical and physical properties and for running seismological synthetics. The D-REX\_M output file(s) includes, for each mineral aggregate, the elastic tensor  $\mathbf{C}$ , density, and the deformation gradient tensor  $\mathbf{F}$ . These properties can be then processed and visualised with the software VIZTOMO (section 2.2.1).

D-REX\_M is parallelized using a hybrid MPI and OpenMP scheme to take advantage of multiple CPUs architectures of modern HPC clusters. Runtime is obviously affected by the number of crystal aggregates, number of crystals per aggregate and of active slip systems per crystal, and number of timesteps (Fig. 5, top). The parallel efficiency is 70-90%, and the update of the LPO and  $\mathbf{F}$  tensor during forward advection is the most time-consuming part of the run (Fig. 5, centre, bottom). The small performance degradation is due to the initialization of the Eulerian/Lagrangian grids and arrays, and to I/O operations which are executed serially within each process. As a result, the efficiency of the time-dependent flow models is lower than that of steady-state models, as the latter only require a single velocity (and  $P$ ,  $T$ ,  $F_d$ ) field to be loaded and processed.



246

247

248 **Figure 5.** Runtime (top), speedup (centre) and parallel efficiency (bottom) of D-REX\_M for initial backward advection of aggregates  
 249 (“backward”), forward advection and updating of the LPO and  $\mathbf{F}$  tensor (“forward”), full elastic tensor computation and output file creation  
 250 (“tensor”), and entire run (“total”). Results are shown for two models included in the cookbooks: the 3Dspherical\_global model (steady-  
 251 state flow, 96 timesteps, 1327606 aggregates, LPO computed only for 260474 upper mantle aggregates) and the 3Dspherical\_sinkingslab  
 252 model (dashed lines; time-dependent flow, 20 timesteps, 38509 aggregates, LPO computed for 25177 upper mantle and 6587 upper mantle  
 253 transition zone aggregates). Runs performed on a HPE Superdome Flex (8 CPUs, 28 cores Intel Xeon(R) PLATINUM 8180 @ 2.50GHz)  
 254 using from 1 to 8 nodes.

255

### 256 2.1.3 EXEV

257 EXEV includes routines to compute the EXtrinsic Elastic and Viscous anisotropy using Effective Medium Theory modelling  
 258 for a multi-component layered system (Smoothed Transversely Isotropic Long-Wavelength Equivalent, STILWE; Backus,  
 259 1962) or a two-component system with similar ellipsoidal inclusions in a uniform background matrix (Differential Effective  
 260 Medium, DEM; e.g., Mainprice, 1997).

261 The elastic tensor  $\mathbf{C}$  due to SPO fabrics can be either estimated independently or, when using the DEM approach, superimposed  
262 on that obtained from the strain-induced LPO modelling. SPO fabrics that can be modelled are those related to rock- or grain-  
263 scale layering (e.g., Faccenda et al., 2019), or to the presence of preferentially aligned ellipsoidal inclusions (e.g., melt-/fluid-  
264 filled cracks). The user then needs to specify:

- 265 • for grain-scale layered fabrics, a dominant ultramafic or mafic lithology. In this case the mineral phase proportions  
266 from the MMA-EoS lookup tables define the mixture for the STILWE model;
- 267 • for rock-scale layered fabrics, the relative abundance of the five available ultramafic-mafic lithologies (dunite,  
268 harzburgite, pyrolite, basalt and pyroxenite) defining the mixture for the STILWE model;
- 269 • for matrix-inclusion fabrics, the elastic tensors of the two components and the inclusion's shape and volume fraction  
270 as required by the DEM modelling. The matrix elastic tensor can be replaced with that from the LPO modelling in  
271 order to estimate the combined effect of LPO and SPO fabrics.

272 The SPO fabrics can then be oriented at any angle relative to the principal Finite Strain Ellipsoid (FSE) axis or, in case of  
273 cracks, the local principal stress obtained from the “present-day” (i.e., last) velocity field.

274 Summarising, SPO fabric modelling requires one or more of the following:  $\mathbf{F}$  and/or  $\mathbf{C}$  obtained from D-REX\_M;  $\mathbf{P}$ ,  $\mathbf{T}$  and/or  
275  $\mathbf{V}$  and/or fluid/melt fraction fields for the “present-day” state of the geodynamic model. Consequently, this modelling is  
276 performed when post-processing the D-REX\_M output with the software VIZTOMO (see section 2.2.1).

277 The total or deviatoric component of the viscous tensor  $\boldsymbol{\eta}$  due to SPO fabrics is estimated for two-phase systems with ellipsoidal  
278 weak/hard inclusions using the DEM theory, and the parametrization of the viscous tensor evolution and orientation as a  
279 function of the cumulated deformation ( $\mathbf{F}$ ) obtained following de Montserrat et al. (2022). Indeed, most if not all, mantle levels  
280 are composed of two main mineral phases that control both the elastic and viscous properties. The case of a multi-component  
281 layered medium is not considered because its viscous tensor can be either approximated with flat inclusions, or more simply  
282 computed using the Voigt and Reuss averages of the layers' isotropic viscosity.

283 The first modelling phase requires running subprogram DEMviscous to generate a database of viscous tensors for a range of  
284 inclusion shapes and volume fractions, and inclusion-matrix viscosity contrasts. The latter implies that the viscous moduli are  
285 dimensionless and can therefore be interpreted as scaling factors with respect to an isotropic effective viscosity of the bulk  
286 rock or most abundant mineral phase. Subsequently, the database can be exploited by large-scale geodynamic simulations to  
287 either (i) return the viscosity tensor  $\boldsymbol{\eta}$  from a look-up table for every point of the computational domain, which can be  
288 superimposed on the isotropic effective viscosity computed from flow laws (coupled mechanical simulations), or (ii) estimate  
289  $\boldsymbol{\eta}$  (uncoupled mechanical simulation) and/or visualise its anisotropic viscous properties for the “present-day” state of the  
290 geodynamic model with the software VIZVISC (section 2.2.2).

291

292 **2.2 Visualisation of the mechanical properties and data formatting in preparation for seismological synthetics**

293 **2.2.1 VIZTOMO**

294 VIZTOMO processes the D-REX\_M output for the visualisation of the aggregates' elastic and deformational history properties.  
295 Estimation of extrinsic anisotropy effects via the EXEV routines is possible at this stage. The properties of the **C** and **F** tensors  
296 can be determined either at the position of the Lagrangian mantle aggregates, or, in case of the elastic properties and density,  
297 interpolated to a structured (tomographic) grid. In the latter case the grid can be saved in a format suitable for generating  
298 synthetic seismic datasets via the PSI\_D package (see section 2.3.2) or for 3D waveform simulations in SPECFEM  
299 (Komatitsch and Tromp, 1999).

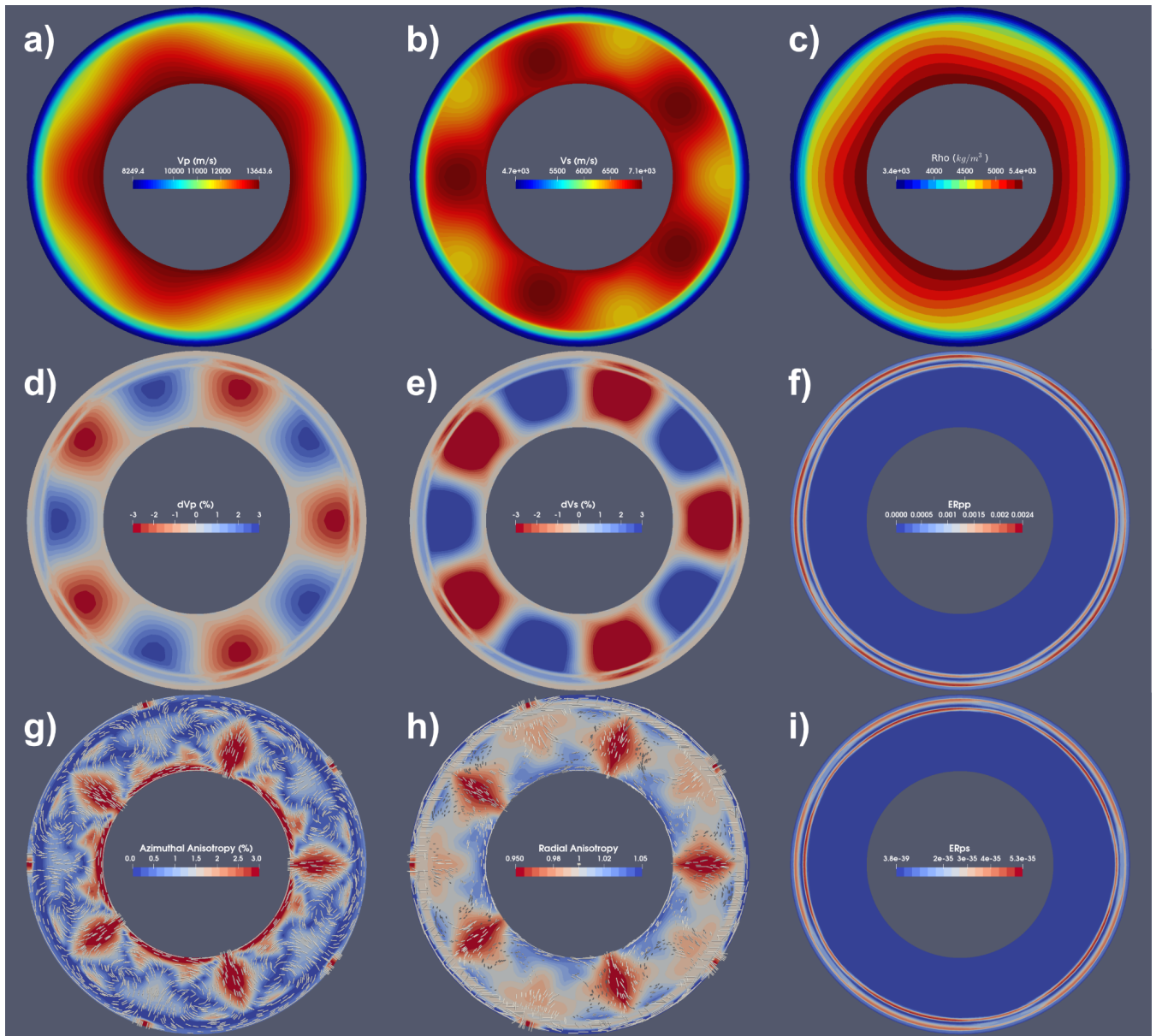
300 Several properties of the elastic tensor **C** can be visualised:

- 301 ● Isotropic or ray-path dependent velocity anomalies and anisotropic elastic properties of body-waves (i.e., P-wave  
302 anisotropy and direction of maximum P-wave velocity; direction and magnitude of maximum S-wave splitting delay  
303 time; S-wave radial and azimuthal anisotropy);
- 304 ● reflection/transmission energies resulting from the whole range of P-S conversions occurring at discontinuities (useful  
305 for studies based on receiver function analysis);
- 306 ● the fraction of the elastic tensor anisotropic component relative to the total and the relative contributions of five  
307 different anisotropy classes (hexagonal, orthorhombic, tetragonal, monoclinic, triclinic) obtained through elastic  
308 tensor decomposition (Browaeys and Chevrot, 2004);
- 309 ● the orientation of the hexagonal symmetry axis (already present in the original D-REX).

310 The deformation history stored in **F** can be visualised in terms of the FSE shape and orientation and/or length or orientation of  
311 its minimum and maximum semi-axes.

312 The different fields are saved in specific file formats which can be imported by the open source ParaView software (Ahrens et  
313 al., 2005) for visualisation. Figures 6, 7, 8, 9 display some of these fields computed for different geodynamic models.

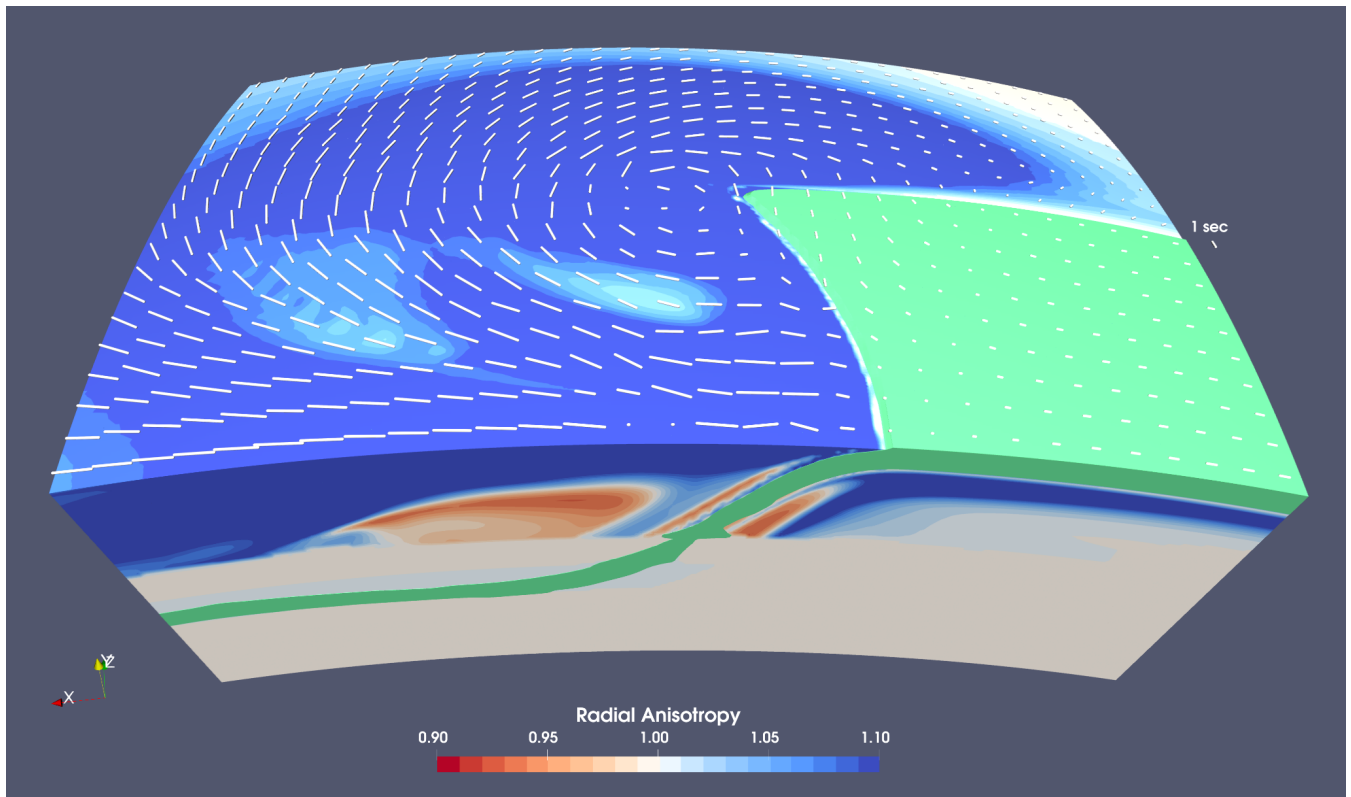
314



315

316 **Figure 6.** VIZTOMO output for the model 2Dpolar\_convection available in the cookbooks. The steady-state 2D incompressible flow field  
 317 in cylindrical coordinates is the result of the analytical solution shown in section 9.3 of the software manual and coded in the MATLAB  
 318 script cookbooks/2Dpolar\_convection/polarcell.m. (a,b) isotropic  $V_p$  and  $V_s$  (m/s); (c) density); (d,e) isotropic P- and S-wave anomalies;  
 319 (g) azimuthal anisotropy and FSE semi-axis (white bars); (h) radial anisotropy and TTI axis (white bars); (f,i) P-P and P-S reflection energy  
 320 for waves propagating upward.



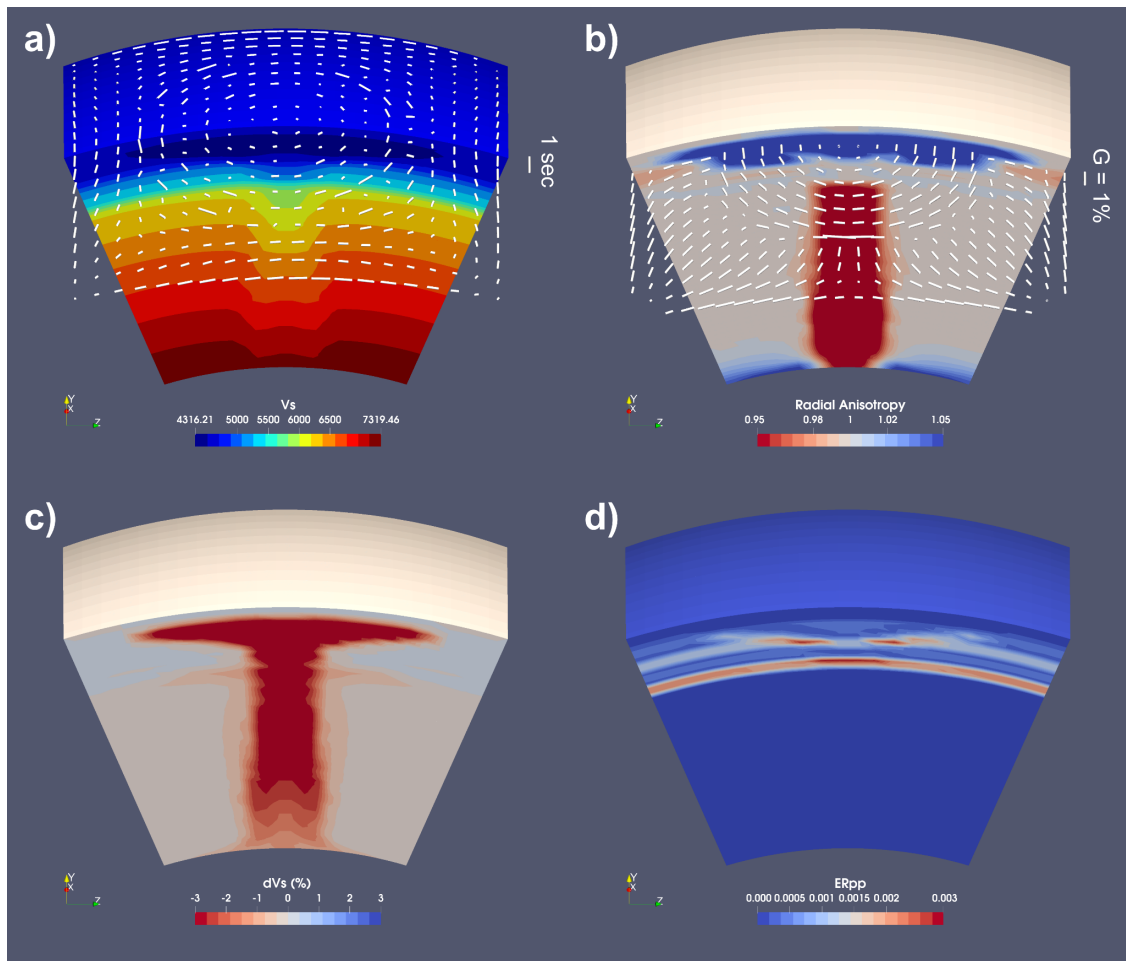


321

322 **Figure 7.** VIZTOMO output for a 3D model of oceanic plate subduction and roll back in spherical coordinates. The time-dependent flow  
 323 field has been computed with the software I3MG modified to account for spherical coordinates (see Faccenda and VanderBeek, 2023).  
 324 Fabrics computed with D-REX\_M for only upper mantle aggregates. A fossil A-type olivine fabric with the fast axis parallel to plate motion  
 325 and computed with D-REX\_S is initially defined within the oceanic plate volume. The colour scale indicates radial anisotropy in the upper  
 326 mantle, and the white bars the SKS splitting computed with SKS-SPLIT. The volume in green encloses material with a +2% P-wave anomaly  
 327 (i.e., the oceanic plate). Note the apparently thicker slab portion around the 410 km depth discontinuity, due to the upwelling of the olivine-  
 328 spinel phase transition. The model domain extends from 0-1000 km along the radial direction, 85°-115° along longitude, and 70-90° along  
 329 colatitude.

330

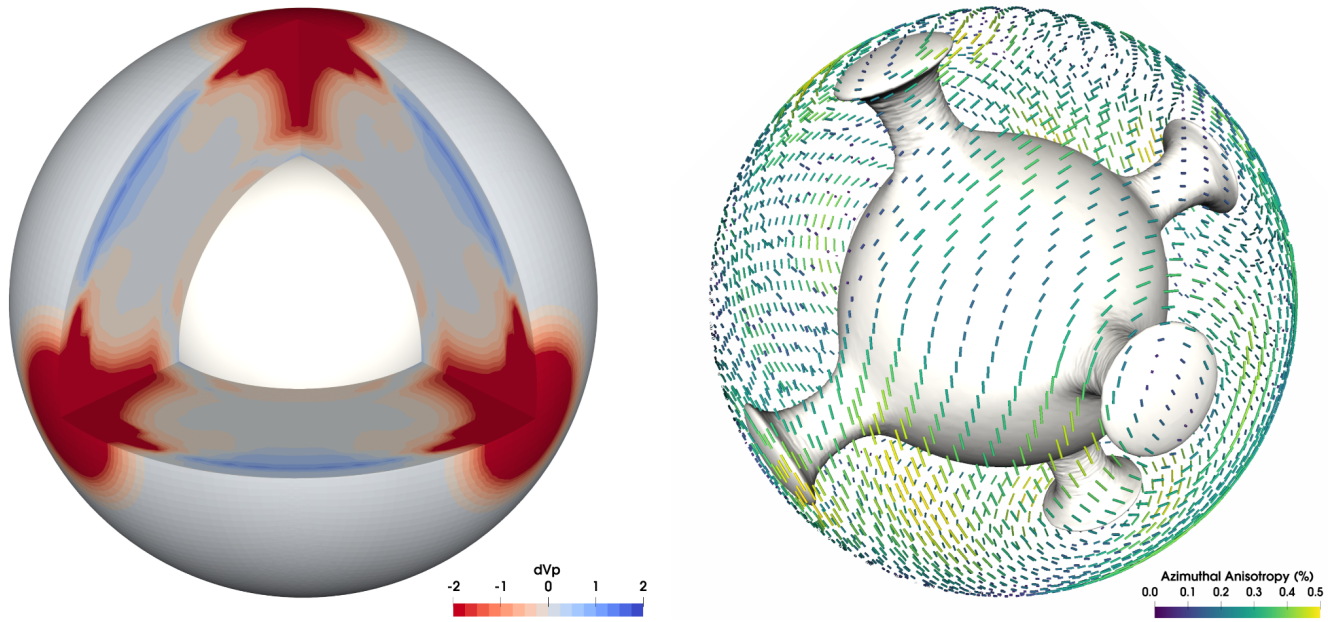
331



332

333 **Figure 8.** VIZTOMO output for an upwelling plume toy model in spherical coordinates. The time-dependent flow field has been computed  
 334 with the software I3MG modified to account for spherical coordinates (see Faccenda and VanderBeek, 2023). a) absolute  $V_s$  (m/s) and SKS  
 335 splitting computed with SKS-SPLIT (white bars); b) radial anisotropy (colour scale) and azimuthal anisotropy at 200 km depth (white bars);  
 336 c) isotropic  $V_s$  anomaly; d) P-P reflection energy for a wave propagating upward. The model domain extends from 0-2900 km along the  
 337 radial direction,  $70^\circ$ - $110^\circ$  along longitude, and  $70^\circ$ - $110^\circ$  along colatitude.

338



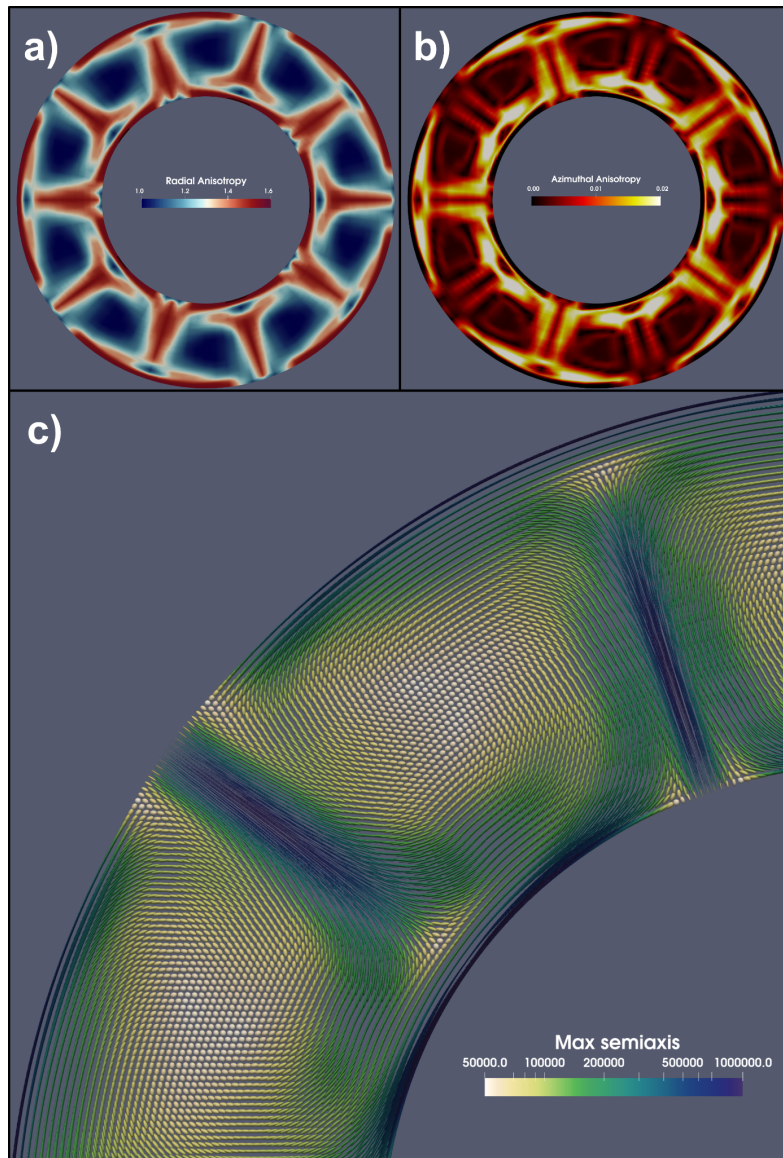
339

340 **Figure 9:** VIZTOMO output for the model 3Dspherical\_global available in the cookbooks. The time-dependent flow field has been computed  
 341 with the software I3MG modified to account for 3D global spherical coordinates using the Yin-Yang grids (Kageyama and Sato, 2004).  
 342 Isotropic P-wave anomaly (left) and azimuthal anisotropy at 200 km depth (right). The grey surface encloses material 0.1 dimensionless  
 343 units hotter than the average temperature at any depth.

344

### 345 2.2.1 VIZVISC

346 VIZVISC processes the D-REX\_M output for the visualisation of the aggregate properties such as the viscous anisotropy and  
 347 related deformational history (in terms of the FSE) in ParaView. The deviation from isotropy is evaluated by computing the  
 348 radial and azimuthal components of viscous anisotropy in a similar way as for the elastic tensor. More in detail, radial viscous  
 349 anisotropy is defined as  $\xi = N/L$ , while azimuthal viscous anisotropy is defined by the magnitude  $G = \sqrt{Gc^2 + Gs^2}$  and  
 350 azimuth  $\phi = \tan^{-1}(Gs, Gc)$ , where  $N = \frac{1}{8}(\eta_{11} + \eta_{22}) - \frac{1}{4}\eta_{12} + \frac{1}{2}\eta_{66}$ ,  $L = \frac{1}{2}(\eta_{44} + \eta_{55})$ ,  $Gc = \frac{1}{2}(\eta_{55} - \eta_{44})$ ,  $Gs = \eta_{45}$ . Radial  
 351 and azimuthal viscous anisotropy are evaluated in the FSE (and thus inclusions) reference frame, whereby the minor semi axis  
 352 is oriented along the vertical direction, and the intermediate and major semi axes are in the horizontal plane. As such, radial  
 353 anisotropy is always  $\geq 1$ . Figure 10 displays some of these fields computed for a 2D steady-state model of mantle convection  
 354 with periodic upwellings and downwellings.



355

356 **Figure 10.** VIZVISC output for the model 2Dpolar\_convection available in the cookbooks. The steady-state 2D incompressible flow field  
 357 in cylindrical coordinates is the result of the analytical solution shown in section 9.3 of the software manual and coded in the MATLAB  
 358 script cookbooks/2Dpolar\_convection/polarcell.m. (a) Radial viscous anisotropy; (b) azimuthal viscous anisotropy; (c) FSE shape coloured  
 359 by the length of its major semi-axis upscaled by a factor of 50 km.

360

## 361 **2.3 Seismic forward and inverse modelling**

### 362 **2.3.1 SKS-SPLIT**

363 SKS-SPLIT estimates the SKS splitting at a grid of virtual seismic stations placed at the top of the D-REX\_M model as a  
364 function of the back-azimuth using the Fortran routines included in FSTRACK (Schulte-Pelkum and Blackmann, 2003; Becker  
365 et al., 2006). These routines use the reflectivity method (for details, see Booth and Crampin, 1983; Chapman and Shearer,  
366 1989) to compute synthetic seismograms through layered anisotropic media traversed by an incident plane wave ( $5^\circ$  for typical  
367 SKS arrivals) over a range of frequencies (0-25 Hz). Band-pass filters from 0.1 to 0.3 Hz are then applied to construct synthetic  
368 seismograms in the SKS band (3.3 to 10s). Successively, the splitting is determined with the cross-correlation method of  
369 Menke and Levin (2003). The routines have been adapted to load the D-REX\_M output, stack the elastic tensors and densities  
370 in an upper mantle rock column beneath each virtual seismic station (Faccenda and Capitanio, 2013), and run in parallel using  
371 MPI. The averaged fast azimuth scaled by the delay time can then be visualised in ParaView as shown in Figures 7 and 8a.

### 372 **2.3.2 PSI**

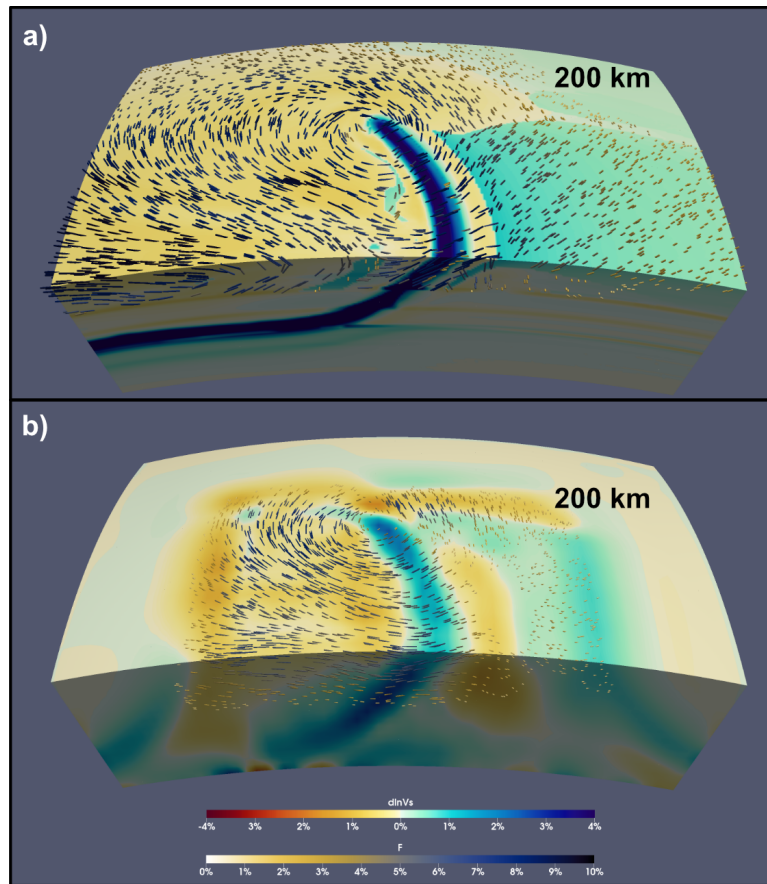
373 PSI (Platform for Seismic Imaging) is a Julia package for performing tomographic inversion of both real and synthetic seismic  
374 datasets. In the context of the ECOMAN software, it's a useful tool for exploring how features in high-resolution geodynamic  
375 simulations are mapped into lower resolution seismic tomography models; this is a critical step if one aims to evaluate  
376 geodynamic results against existing tomographic images.

377 PSI can be used to forward model P and S travel-times, splitting intensity (Chevrot, 2000), and shear wave splitting parameters  
378 (i.e. the fast-polarisation azimuth and the delay time between the fast- and slow-polarised waveforms). Forward modelling of  
379 these seismic observables is supported for three different model parameterizations: (1) isotropic P- and S-wavespeeds, (2)  
380 hexagonally anisotropic media defined by the 5 Thomsen parameters and the azimuth and elevation of the symmetry axis, and  
381 (3) fully anisotropic models defined by the density-normalised 21-component elastic tensor which can be generated from D-  
382 REX\_M + VIZTOMO (sections 2.1.2 and 2.2.1). Seismic phase velocities are computed following Thomsen (1986) for  
383 hexagonally anisotropic models while the Christoffel equations are solved when the elastic tensor parameterization is used.  
384 Anisotropic travel-times and splitting intensities for arbitrarily polarised S-waves are computed following VanderBeek et al.  
385 (2023) using a long-wavelength approximation in which the accumulated delay time between fast- and slow-polarised qS-  
386 waves is less than their dominant period. Lastly, splitting parameters are predicted using the matrix propagation method of  
387 Rumpker and Silver (1998). In this initial release of PSI, all predictions are made via integration along ray paths traced through  
388 a user-defined 1D reference velocity model using the TauP Toolkit (Crotwell et al. 1998). The 3D model properties are  
389 subsequently interpolated to these paths before computing the seismic observables. We anticipate releasing an update to the  
390 package that includes both 3D anisotropic ray tracing and finite-frequency kernels that are currently under development.

391 Travel-time and splitting intensity datasets can be inverted individually and jointly either for isotropic ( $V_p$  and  $V_s$ ) or  
392 hexagonally anisotropic model parameters. Hexagonal anisotropy is defined by up to five free parameters, the isotropic (1) P-

393 and (2) S-velocity, (3) anisotropic magnitude, and the (4) azimuth and (5) elevation of the hexagonal symmetry axis. Only a  
394 single anisotropic magnitude parameter is required because the strength of P and S anisotropy is strongly correlated (e.g.,  
395 Becker et al., 2006). Consequently, the ratios between the three Thomsen parameters ( $\epsilon$ ,  $\delta$ ,  $\gamma$ ; Thomsen 1986) and the inverted  
396 anisotropic magnitude parameter must be chosen *a priori* and can be spatially variable. Source and receiver statics for each  
397 observation and seismic phase type may also be included as free parameters. The tomographic model is obtained by iteratively  
398 solving a system of linearized equations relating the perturbations in the inversion parameters to the data residuals augmented  
399 with damping and smoothing constraints. The solution is obtained via the LSQR algorithm (Paige & Saunders, 1982). Full  
400 details on the tomographic method can be found in VanderBeek and Faccenda (2021) and VanderBeek et al. (2023). The final  
401 tomographic solution is written to a VTK file to be visualised in ParaView. Tomographic inversions can be run from a  
402 workstation. For the problem shown in Figure 11 and consisting of 12,320 observations and 415,044 free parameters, solutions  
403 can be obtained within ~10 minutes (less for isotropic inversions) using 6 cores and 1.8 GB peak RAM.

404 The PSI inversion methodology has been tested on synthetic models of oceanic plate subduction, intra-oceanic upwelling  
405 plume, spreading oceanic ridge, and Central-Eastern Mediterranean subduction (VanderBeek and Faccenda, 2021; Lo Bue et  
406 al., 2022, VanderBeek et al., 2023; Faccenda and VanderBeek, 2023), and applied to the isotropic and anisotropic imaging of  
407 the Central Mediterranean (Rappisi et al., 2022) and of the Mt. Etna volcanic field (Lo Bue et al., 2024). In Figure 11, we  
408 illustrate results obtained from a synthetic inversion of direct teleseismic P- and S-wave relative travel-times computed through  
409 the subduction zone shown in Figure 7. Synthetic data were computed using the full 21-component elastic tensor while the  
410 inversion was performed for the best-fit hexagonal anisotropic parameters. We considered an array of 770 receivers extending  
411 from  $\pm 7.5^\circ$  in longitude and  $\pm 11.5^\circ$  in latitude (~75 km spacing) that recorded 16 events; 8 at a range  $50^\circ$  and another 8 at  $80^\circ$   
412 from the origin of the subduction zone model and equally distributed in back-azimuth. This example is included in the PSI  
413 package.



414

415 **Figure 11.** Synthetic tomography results obtained from PSI for the model shown in Fig. 7. (a) Target anisotropic model generated from  
 416 VIZTOMO. (b) Recovered anisotropic model obtained by inverting synthetic teleseismic P and S (relative) delay times computed from the  
 417 model in (a). In both panels, the isotropic S-wave velocity perturbations are computed with respect to the far-field 1D velocity profile.  
 418 Quivers parallel the hexagonal symmetry axis and are scaled and coloured by the anisotropic strength. The top surface shown is located at  
 419 200 km depth while the full model extends from 0-1000 km along the radial direction,  $85^\circ$ - $115^\circ$  along longitude, and  $0$ - $20^\circ$  along latitude.

## 420 3 Discussion

### 421 3.1 Software advantages

422 When compared to other similar software, ECOMAN (i) aims at being a more versatile package suitable for any geodynamic  
 423 simulations (2D and 3D; Cartesian and polar coordinate systems; regional and global settings), (ii) takes into account the time-  
 424 dependent deformational history of the mantle (which is usually not steady-state, especially close to plate boundaries), (iii)  
 425 predicts the strain-induced fabric and elastic tensor of different mantle layers (i.e., not only the upper mantle), (iv) includes  
 426 Effective Medium Theories (STILWE, DEM) and a parametrization of the fabric evolution of two-phase composites to predict  
 427 elastic and viscous extrinsic anisotropy, (v) generates realistic grid structure distributions of mantle elastic properties to be  
 428 used for forward/inverse seismological modelling (e.g., PSI, SPECFEM3D), and (vi) performs synthetic seismic inversions  
 429 (e.g., P- and S-wave travel-time tomographies, S-wave splitting intensities) within the computational domain, which facilitates

430 the comparison with other tomographic models and the estimation of apparent anomalies (artefacts) due to, for example,  
431 unaccounted-for elastic anisotropy (Bezada et al., 2016; VanderBeek and Faccenda, 2021; VanderBeek et al., 2023) and/or  
432 regularisation.

### 433 **3.2 Software (real or potential) current limitations**

434 D-REX\_S and D-REX\_M compute the strain-induced LPO for the most abundant and highly anisotropic mineral phases, while  
435 assuming random orientation for several secondary phases that instead could contribute substantially to the aggregate  
436 anisotropic properties. For example, cubic ferropericlasite is relatively abundant (< 20%) and becomes highly anisotropic in the  
437 lower half of the lower mantle ( $A_{vs} = 30\text{-}50\%$ ), such that it could dominate seismic anisotropy at these depths (Marquardt et  
438 al., 2009). Davemaoite (Ca-perovskite) is also a highly anisotropic mineral with cubic symmetry ( $A_{vs} = 25\text{-}15\%$ , Kawai and  
439 Tsuchiya, 2015) but its model abundance is quite low (< 10%). Recently, micromechanical simulations of strain-induced LPO  
440 in aggregates with a pyrolite mantle composition have shown that the bulk aggregate seismic anisotropy is controlled by  
441 bridgmanite and post-perovskite, while the cubic secondary phases appear to only slightly reduce the amplitude of anisotropy  
442 (Chandler et al., 2021). The latter effect can thus be well approximated by randomising the orientation of the cubic phases as  
443 assumed here.

444 A main limitation of ECOMAN is that it does not include yet the modelling of viscous anisotropy due to the intrinsic  
445 mechanical anisotropy of crystals. Tommasi et al. (2009), have used VPSC simulations to show that olivine CPO in the  
446 lithosphere can control the reactivation of fossil faults misoriented with respect to the stress field. Kiraly et al (2020), employed  
447 the modified director method (MDM) and estimated up to 1 order of magnitude of intrinsic viscous anisotropy in olivine  
448 aggregates, which can control the kinematics and dynamics of tectonic plates. Both the VPSC and MDM approaches are  
449 computationally expensive and appear to be prohibitive for the number of mantle aggregates required to discretize the mantle  
450 domain of large-scale 3D simulations. An alternative approach which minimises the computational time is therefore desired.  
451 Fraters and Billen (2021) have released a version of the D-REX model that is embedded into the ASPECT geodynamic  
452 modelling software (Banghart et al., 2020) and that takes into account changes in olivine fabric as a function of the water  
453 content and deviatoric stress (Karato et al., 2008). Although at present D-REX\_M only allows the definition of a single olivine  
454 fabric per run, changes in crystal fabrics can be easily implemented in the future by loading the water content and deviatoric  
455 stress field from the geodynamic models and by parametrizing the boundaries of the olivine fabric domains.

456 Tape and Tape (2024) recently reformulated the elastic decomposition method proposed by Browaeys and Chevrot (2004) that  
457 they argued is not entirely accurate. Although this will only affect the visualization of the tensor components as performed by  
458 D-REX\_S and VIZTOMO, it is planned to replace the existing elastic tensor decomposition methodology with the one  
459 proposed by Tape and Tape (2024).

460 A minor limitation is that the different code modules are based on different programming languages (Fortran, Julia), libraries  
461 (OpenMP, MPI, HDF5) and software (MATLAB, ParaView), whose installation on local devices might discourage potential



462 users. There are a few main reasons for this. First of all, the original D-REX software was written in Fortran, thus its  
463 modifications into D-REX\_S and D-REX\_M software was more straightforward by maintaining the same programming  
464 language. Fortran has high performance standards on HPC clusters, often if not always higher than other interpreted  
465 programming languages (e.g., MATLAB or Python). Given the large-scale computational power needed for the D-REX\_M  
466 simulations, especially those with 100,000s or millions of crystal aggregates, and considering that the required compilers and  
467 libraries are routinely installed in most (if not all) HPC clusters, the usage of the ECOMAN's Fortran-based applications in  
468 high-performance environments is warranted. In contrast, the visualisation of the Fortran-based applications' output in  
469 MATLAB and ParaView can be performed on local devices. In particular, the MTEX software is a MATLAB toolbox for  
470 visualisation of the LPO and elastic tensor pole figures which should be downloaded ([https://mtex-  
471 toolbox.github.io/download](https://mtex-toolbox.github.io/download)) and installed along with MATLAB only when using D\_REX\_S. Seismic forward/inverse  
472 modelling with PSI can be performed on either a HPC cluster or local devices upon installation of the Julia package. Julia was  
473 chosen because it is an open-source and high-level language that offers a number of performance benefits over other popular  
474 scientific computing languages such as Python or Matlab. It is important to stress that for any of these applications the user  
475 only needs to modify input text files, and thus no particular prerequisite or computational skill is required.  
476 Finally, running D-REX\_M requires allocating ~ 160 GB of memory per million of crystal aggregates with 1000 x 2 crystals  
477 each. This potential problem can be addressed by distributing the computational and memory load over several nodes, which  
478 is possible thanks to the hybrid MPI and OpenMP parallelization scheme.

#### 479 **4 Conclusions and outlook**

480 ECOMAN is an open-source software package for estimating strain/stress-induced fabrics in mantle aggregates, their  
481 mechanical properties, and how mechanical anisotropy affects the geodynamic evolution and seismic imaging of the Earth's  
482 interior. Programs included in ECOMAN are portable across different HPC and local device systems (provided the Julia  
483 package and Fortran compilers are available), and are applicable to any 2D-3D geodynamic simulation. Computationally  
484 expensive programs such as D-REX\_M are parallelized, offering a nearly perfect scaling with an increasing number of cores.  
485 As a result, the strain-induced fabrics of millions of mantle aggregates can now be estimated with a reasonable amount of time  
486 and computational resources.

487 As ongoing developments, we are seeking to include in ECOMAN micromechanical modelling methods that are capable of  
488 estimating the strain-induced LPO and/or the intrinsic viscous anisotropy at computational speeds that are orders of magnitude  
489 faster than current ones. For instance, Ribe et al. (2019), have proposed an analytical finite-strain parameterization for texture  
490 evolution in deforming olivine polycrystals that is  $\approx 10^7$  times faster than full homogenization approaches such as the second-  
491 order self-consistent model. When implemented in ECOMAN, preliminary tests indicate that this new method outperforms D-  
492 REX by 1-2 orders of magnitude (Ribe et al., 2023).

493 In addition, in the near future the PSI software will be updated to include trans-dimensional Bayesian Monte Carlo sampling  
494 methods that, in contrast to deterministic approaches, address the consequences of under-determination in seismic imaging by  
495 constraining the uncertainty (Del Piccolo et al., 2023). Isotropic and anisotropic seismic imaging with PSI is currently feasible  
496 using body wave information such as travel-times and S-wave splitting intensity. However, when local deep seismicity is  
497 absent, as is the case in warm subduction zones or at spreading ridges and intraplate settings, the retrieved isotropic and  
498 anisotropic mantle structures are only partially recovered and often affected by smearing (e.g., Faccenda and VanderBeek,  
499 2023). Consequently, we are planning to complement body wave information with surface wave data to improve the seismic  
500 ray coverage and the resolving power of tomographic models. Lastly, to improve the prediction of seismic observables, 3D  
501 anisotropic ray tracing and finite-frequency kernels are planned for a future release.

## 502 **Code availability**

503 The version of ECOMAN described in this article is 2.0 and is freely available at github (<https://github.com/ecoman-geos>) and  
504 zenodo (ECOMAN2.0-geodynamics: <https://doi.org/10.5281/zenodo.10599735>; ECOMAN2.0-seismology.SKS-split: <https://doi.org/10.5281/zenodo.11173260>;  
505 ECOMAN2.0-seismology.PSI\_D: <https://doi.org/10.5281/zenodo.11186805> ).

## 506 **Data availability**

507 The software package contains the input files to generate the synthetic models and datasets discussed in this manuscript. No  
508 data has been produced for this work.

## 509 **Author contributions**

510 MF and BPV developed the software package, with important contributions from AdM, JY and FR. MF wrote the manuscript  
511 draft. MF acquired the funding supporting the research activities. All authors have contributed to the discussion and manuscript  
512 editing.

## 513 **Competing interests**

514 The authors declare that they have no conflict of interest.

515 **Acknowledgements**

516 MF is indebted to F.A. Capitanio for supporting the beginning of this journey, T.W. Becker for providing routines to compute  
517 shear wave splitting, E. Kaminski for fruitful discussions on strain-induced LPO modelling, and to A.M. Ferreira for the  
518 continuous and stimulating feedback. Two anonymous reviewers helped in improving the article.

519 **Financial statement**

520 This study is supported by the ERC StG 758199 NEWTON.

521 **References**

- 522 Abt, D. L., Fischer, K. Resolving three-dimensional anisotropic structure with shear wave splitting tomography. *Geophys. J.*  
523 *Int.* 173, 859-886, 2008.
- 524 Ahrens, J., Geveci, B., and Law, C.: ParaView: An End-User Tool for Large Data Visualization, in: *Visualization Handbook*,  
525 edited by: Hansen, C.D. and Johnson, C.R., Elsevier, 717-731, <https://doi.org/10.1016/B978-012387582-2/50038-1>,  
526 2005.
- 527 Almqvist, B.S.G. and Mainprice, D. Seismic properties and anisotropy of the continental crust: Predictions based on mineral  
528 texture and rock microstructure. *Rev. Geophys.*, 55, 367–433, <https://doi.org/10.1002/2016RG000552>, 2017.
- 529 Bangerth, W., Dannberg, J., Gassmoeller, R., & Heister, T. (2020). *Aspect v2.2.0*. *Zenodo*.  
530 <https://doi.org/10.5281/zenodo.3924604>.
- 531 Becker, T.W., Chevrot, S., Schulte-Pelkum, V. and Blackman, D.K.: Statistical properties of seismic anisotropy predicted by  
532 upper mantle geodynamic models. *J. Geophys. Res.*, 111, B08309 <https://doi.org/10.1029/2005JB004095>, 2006.
- 533 Bezada, M., Faccenda, M. and Toomey, D. R: Representing anisotropic subduction zones with isotropic velocity models: A  
534 characterization of the problem and some steps on a possible path forward. *Geochem. Geophys. Geosyst.*,  
535 <https://doi.org/10.1002/2016GC006507>, 2016.
- 536 Booth, D. C., and S. Crampin. The anisotropic reflectivity technique: Theory, *Geophys. J. R. Astron. Soc.*, 72, 31–45, 1983.
- 537 Browaeys, J.T. and Chevrot, S.: Decomposition of the elastic tensor and geophysical applications. *Geophys. J. Int.*, 159, 2,  
538 667–678, 2004.
- 539 Bunge, H.-P., Hagelberg, C.R. and Travis, B.J.: Mantle circulation models with variational data assimilation: inferring  
540 past mantle flow and structure from plate motion histories and seismic tomography. *Geophys. J. Int.*, 152, 280–301,  
541 2003.
- 542 Chandler, B.C., Chen, L.-W., Li, M., Romanowicz, B. and Wenk, H.-R.: Seismic anisotropy, dominant slip systems and phase  
543 transitions in the lowermost mantle. *Geophys. J. Int.*, 227, 1665-1681, <https://doi.org/10.1093/gji/ggab278>, 2021.

544 Chang, S.-J., Ferreira, A. M. G., Ritsema, J., van Heijst, H. J. and Woodhouse, J. H. Joint inversion for global isotropic and  
545 radially anisotropic mantle structure including crustal thickness perturbations. *Journal of Geophysical Research: Solid*  
546 *Earth*, 120, 4278–4300. <https://doi.org/10.1002/2014JB011824>, 2015

547 Chang, S.-J., Ferreira, A.M.G. and Faccenda, M. Upper- and mid-mantle interaction between the Samoan plume and the Tonga-  
548 Kermadec slabs. *Nat. Commun.*, 7:10799, <https://doi.org/10.1038/ncomms10799>, 2016.

549 Chapman, C. H., Shearer, P.M. Ray tracing in azimuthally anisotropic media: II. Quasishear wave coupling, *Geophys. J. Int.*,  
550 96, 65–83, 1989.

551 Chust, T.C., Steinle-Neumann, G., Dolejs, D., Schuberth, B.S. and Bunge, H.P.: MMA- EoS: a computational framework for  
552 mineralogical thermodynamics. *J. Geophys. Res.* 122, 9881–9920, 2017.

553 Cramer, F., and Tackley, P. J. Spontaneous development of arcuate single-sided subduction in global 3-D mantle convection  
554 models with a free surface. *J. Geophys. Res. Solid Earth*, 119, 921–5942, <https://doi.org/10.1002/2014JB010939> , 2014.

555 Davies, D.R., Goes, S., Davies, J.H., Schuberth, B.S.A., Bunge, H.-P. and Ritsema, J.. Reconciling dynamic and seismic  
556 models of Earth's lower mantle: The dominant role of thermal heterogeneity. *Earth Planet. Sci. Lett.*, 353–354, 253-  
557 269, 2012.

558 de Montserrat, A., Faccenda, M., and Pennacchioni, G.: Extrinsic anisotropy of two-phase Newtonian aggregates: Fabric  
559 characterization and parameterization. *J. Geophys. Res.: Solid Earth*, 126, e2021JB022232.  
560 <https://doi.org/10.1029/2021JB022232>, 2021.

561 Debayle, E., Kennet, B., Priestley, K. Global azimuthal seismic anisotropy and the unique plate-motion deformation of  
562 Australia. *Nature* 433, 509-512, 2005.

563 Debayle, E., Bodin, T., Durand, S. and Ricard, Y.. Seismic evidence for partial melt below tectonic plates. *Nature* 586, 555–  
564 559. <https://doi.org/10.1038/s41586-020-2809-4>, 2020.

565 Del Piccolo, G., VanderBeek, B., Faccenda, M., Morelli, A., and Byrnes, J.: Reversible-Jump, Markov-Chain Monte Carlo  
566 seismic tomographic inversion for anisotropic structure in subduction zones (No. EGU23-9927). *Copernicus*  
567 *Meetings*, <https://doi.org/10.5194/egusphere-egu23-9927>, 2023.

568 Deuss, A. Heterogeneity and anisotropy of Earth's inner core. *Annu. Rev. Earth. Planet. Sci.* 42, 103–126,  
569 <https://doi.org/10.1146/annurev-earth-060313-054658>, 2014.

570 Faccenda M. and Capitanio, F. A.: Development of mantle seismic anisotropy during subduction-induced 3D flow. *Geophys.*  
571 *Res. Lett.*, 39, <https://doi.org/10.1029/2012GL051988>, 2012.

572 Faccenda M. and Capitanio, F. A.: Seismic anisotropy around subduction zones: insights from three-dimensional modeling of  
573 upper mantle deformation and SKS splitting calculations. *Geochem. Geophys. Geosyst.*,  
574 <https://doi.org/10.1002/ggge.20055>, 2013.

575 Faccenda, M.: Mid mantle seismic anisotropy around subduction zones, *Phys. Earth Planet. Int.*, 227, 1–19., 2014

576 Faccenda, M., Ferreira, A.M.G., Tisato, N., Lithgow-Bertelloni, C., Stixrude, L. and Pennacchioni, G.: Extrinsic anisotropy in  
577 a compositionally heterogeneous mantle. *J. Geophys. Res.* 124, <https://doi.org/10.1029/2018JB016482>, 2019.

578 Ferreira, A.M.G., Faccenda, M., Sturgeon, W., Chang, S.-J. and Schardong, L.: Ubiquitous lower-mantle anisotropy beneath  
579 subduction zone. *Nature Geo.* 12, 301-306, <https://doi.org/10.1038/s41561-019-0325-7>, 2019.

580 Faccenda, M. and VanDerBeek, B.P.: On constraining 3D seismic anisotropy in subduction, mid-ocean-ridge, and plume  
581 environments with teleseismic body wave data. *J. Geodyn.*, 158, <https://doi.org/10.1016/j.jog.2023.102003>, 2023.

582 Fraters, M. R. T. and Billen, M. I.: On the implementation and usability of crystal preferred orientation evolution in  
583 geodynamic modeling. *Geochem., Geophys., Geosys.*, 22, e2021GC009846. <https://doi.org/10.1029/2021GC009846>,  
584 2021.

585 French, S., and Romanowicz, B. Broad plumes rooted at the base of the Earth's mantle beneath major hotspots. *Nature* 525,  
586 95–99, <https://doi.org/10.1038/nature14876>, 2015.

587 Jadamec, M. and Billen, M.: Reconciling surface plate motions with rapid three-dimensional mantle flow around a slab edge.  
588 *Nature* 465, 338–341, <https://doi.org/10.1038/nature09053>, 2010.

589 Kageyama, A. and Sato, T: “Yin-Yang grid”: An overset grid in spherical geometry. *Geochem Geophys. Geosys.*, 5, 9,  
590 <https://doi.org/10.1029/2004GC000734>, 2004.

591 Kaminski, E., Ribe, N. M. and Browaeys, J. T.: D-Rex, a program for calculation of seismic anisotropy due to crystal  
592 lattice preferred orientation in the convective upper mantle. *Geophys. J. Int.*, 158(2), 744–752.  
593 <https://doi.org/10.1111/j.1365-246x.2004.02308.x>, 2004.

594 Karato, S.-I.: Seismic anisotropy in the deep mantle, boundary layers and the geometry of mantle convection. *Pure and Applied*  
595 *Geophysics*, 151(2-4), 565–587. <https://doi.org/10.1007/s000240050130>, 1998.

596 Karato, S.-i., Jung, H., Katayama, I., and Skemer, P. Geodynamic significance of seismic anisotropy of the upper mantle:  
597 New insights from laboratory studies. *Annual Review of Earth and Planetary Sciences*, 36(1), 59–95.  
598 <https://doi.org/10.1146/annurev.earth.36.031207.124120> , 2008.

599 Kawai, K. and Tsuchiya, T.: Small shear modulus of cubic CaSiO<sub>3</sub> perovskite. *Geophys. Res. Lett.*, 42, 8,  
600 <https://doi.org/10.1002/2015GL063446>, 2015.

601 Kendall, J.-M.: Seismic anisotropy in the boundary layers of the mantle. In *Earth's deep interior: Mineral physics and*  
602 *tomography from the atomic to the global scale*, Geophysical Monograph Series, 117, 133–159, Washington, DC:  
603 American Geophysical Union, 2000.

604 Kim, E., Kim, Y. and Mainprice, D.: AnisEulerSC: A MATLAB program combined with MTEX for modeling the anisotropic  
605 seismic properties of a polycrystalline aggregate with microcracks using self-consistent approximation. *Comp. &*  
606 *Geosci.*, 145, 104589, <https://doi.org/10.1016/j.cageo.2020.104589>, 2020.

607 Király, Á., Conrad, C. P. and Hansen, L. N.: Evolving viscous anisotropy in the upper mantle and its geodynamic implications.  
608 *Geochem. Geophys., Geosys.*, 21, e2020GC009159, <https://doi.org/10.1029/2020GC009159>, 2020.

609 Kocher, T. Schmalholz, S.M. and Mancktelow, N.S. Impact of mechanical anisotropy and power-law rheology on single layer  
610 folding. *Tectonophys.* 421, 1-2, 71-87, 2006.

611 Komatitsch, D. and Tromp, J.: Introduction to the spectral element method for three-dimensional seismic wave propagation,  
612 Geophys. J. Int., 139(3), 806–822, 1999.

613 Halter, W., Macherel, E., Duretz, T., and Schmalholz, S. M. Numerical modelling of strain localization by anisotropy evolution  
614 during 2D viscous simple shearing, EGU General Assembly 2022, Vienna, Austria, 23–27 May 2022, EGU22-11438,  
615 <https://doi.org/10.5194/egusphere-egu22-11438>, 2022.

616 Hansen, L. N., Zhao, Y.-H., Zimmerman, M. E., Kohlstedt, D.L., Protracted fabric evolution in olivine: Implications for the  
617 relationship among strain, crystallographic fabric, and seismic anisotropy. Earth Planet. Sci. Lett. 387, 157-168,  
618 <https://doi.org/10.1016/j.epsl.2013.11.009>, 2014.

619 Hedjazian, N., Garel, F., Rhodri Davies, D. and Kaminski: E. Age-independent seismic anisotropy under oceanic plates  
620 explained by strain history in the asthenosphere. Earth Planet. Sci. Lett. 460, 135-142, 2017.

621 Hu, J., Faccenda, M. and Liu, L.. Subduction-controlled mantle flow and seismic anisotropy in South America. Earth and  
622 Planet. Sci. Lett. 470, 13-24, <https://doi.org/10.1016/j.epsl.2017.04.027>, 2017

623 Li, Z.-H., Di Leo, J.F. and Ribe, N. M. Subduction-induced mantle flow, finite strain, and seismic anisotropy: Numerical  
624 modeling, J. Geophys. Res. Solid Earth, 119, 5052–5076, <https://doi.org/10.1002/2014JB010996>, 2014.

625 Lo Bue, R., Faccenda, M. and Yang, J.: The role of Adria Plate Lithospheric Structures on the Recent Dynamics of the Central  
626 Mediterranean Region. J. Geophys. Res., 126, e2021JB022377. <https://doi.org/10.1029/2021JB022377>, 2021.

627 Lo Bue, R., Rappisi, F., VanderBeek, B.P. and Faccenda, M.: Tomographic Image Interpretation and Central-Western  
628 Mediterranean-Like Upper Mantle Dynamics From Coupled Seismological and Geodynamic Modeling Approach.  
629 Front. Earth Sci., 10:884100, <https://doi.org/10.3389/feart.2022.884100>, 2022.

630 Lo Bue, R., Rappisi, F., Firetto Carlino, M., Giampiccolo, E., Cocina, O., Vanderbeek, B. P. and Faccenda, M. Crustal  
631 structure of Etna volcano (Italy) from P-wave anisotropic tomography. Geophys. Res. Lett. 51, e2024GL108733,  
632 <https://doi.org/10.1029/2024GL108733>, 2024.

633 Long, M.D. and Becker, T.W.: Mantle dynamics and seismic anisotropy. Earth Planet. Sci. Lett., 297, 341-354, 2010.

634 Long, M.D., Maarten V., Van Der Hilst, R.D. Wave-equation shear wave splitting tomography. Geophys. J. Int. 172 (1), 311-  
635 330, <https://doi.org/10.1111/j.1365-246X.2007.03632.x>, 2008.

636 Maguire, R., Ritsema, J., Bonnin, M., van Keken, P. E. and Goes, S.: Evaluating the resolution of deep mantle plumes in  
637 teleseismic travelttime tomography. J. Geophys. Res., 123, 384–400. <https://doi.org/10.1002/2017JB014730>, 2018.

638 Mainprice, D.: Modelling the anisotropic seismic properties of partially molten rocks found at mid-ocean ridges. Tectonophysics,  
639 279, 1-4, 161-179, 1997.

640 Mainprice, D., Hielscher, R. and Schaeben, H.: in Prior, D.J., Rutter, E.H., Tatham, D. J. Calculating anisotropic physical  
641 properties from texture data using the MTEX open source package. (eds) Deformation Mechanisms, Rheology and  
642 Tectonics: Microstructures, Mechanics and Anisotropy. Geological Society, London, Special Publications, 360, 175-  
643 192, 2011.

644 Marquardt, H., Speziale, S., Reichmann, H. J., Frost, D. J., Schilling, F. R. and Garnero, E.J.: Elastic Shear Anisotropy of  
645 Ferropericlasite in Earth's Lower Mantle. *Science*, 324, 5924, 224-226, <https://doi.org/10.1126/science.1169365>, 2009

646 Menke, W., Levin, V. The cross-convolution method for interpreting SKS splitting observations, with application to one and  
647 two layer anisotropic earth models, *Geophys. J. Int.*, 154, 379–392, 2003.

648 Mondal, P., Long, M.D. A model space search approach to finite-frequency SKS splitting intensity tomography in a reduced  
649 parameter space. *Geophys. J. Int.* 217, 238-256, <https://doi.org/10.1093/gji/ggz016>, 2019.

650 Müller, R. D., Flament, N., Cannon, J., Tetley, M. G., Williams, S. E., Cao, X., Bodur, Ö. F., Zahirovic, S., and Merdith, A.:  
651 A tectonic-rules-based mantle reference frame since 1 billion years ago – implications for supercontinent cycles and  
652 plate–mantle system evolution, *Solid Earth*, 13, 1127–1159, <https://doi.org/10.5194/se-13-1127-2022>, 2022.

653 Munzarová, H., Plomerová, J., Kissling, E.. Novel anisotropic teleseismic body- wave tomography code AniTomo to  
654 illuminate heterogeneous anisotropic upper mantle: Part I–theory and inversion tuning with realistic synthetic data.  
655 *Geophys. J. Int.* 215 (1), 524–545, 2018.

656 Oganov, A.R. and Ono, S.: Theoretical and experimental evidence for a post-perovskite phase of MgSiO<sub>3</sub> in Earth's D'' layer.  
657 *Nature*, 430, 445–448, 2004.

658 Rappisi, F., VanderBeek, B., Faccenda, M., Morelli, A. and Molinari, I: Slab geometry and upper mantle flow patterns in the  
659 Central Mediterranean from 3D anisotropic P-wave tomography. *J. Geophys. Res.* 127, e2021JB023488,  
660 <https://doi.org/10.1029/2021JB023488>, 2022.

661 Ribe, N.M., Hielscher, R.H. and Castelnau, O.: An analytical finite-strain parameterization for texture evolution in deforming  
662 olivine polycrystals. *Geophys. J. Int.*, 216, 486–514, <https://doi.org/10.1093/gji/ggy442>, 2019.

663 Ribe, N.M., Faccenda, M., Hielscher, R.H.: SBFTEX: An Analytical Parameterization for Finite Strain-Induced Upper-Mantle  
664 Anisotropy. AGU Fall Meeting 2023, DI42A-08, 2023.

665 Rudolph, M.L., Lekić, V. and Lithgow-Bertelloni, C.: Viscosity jump in Earth's mid-mantle. *Science*, 350, 1349-  
666 1352, <https://doi.org/10.1126/science.aad1929> , 2015.

667 Schaeffer, A.J., Lebedev, S. and Becker, T.W. Azimuthal seismic anisotropy in the Earth's upper mantle and the thickness of  
668 tectonic plates. *Geophys. J. Int.*, 207, 2, 901–933, <https://doi.org/10.1093/gji/ggw309>, 2016.

669 Schuberth, B.S.A., Zaroli, C. and Nolet, G.: Synthetic seismograms for a synthetic Earth: long-period P- and S-wave traveltime  
670 variations can be explained by temperature alone, *Geophys. J. Int.*, 188(3), 1393–1412, doi:10.1111/j.1365-  
671 246X.2011.05333.x, 2012.

672 Schulte-Pelkum, V. and Blackman, D.K.: A synthesis of seismic P and S anisotropy, *J. Geophys. Int.*, 154, 1, 166–178, 2003.

673 Shea Jr, W. T. and Kronenberg, A. K. Strength and anisotropy of foliated rocks with varied mica contents. *Journal of Structural*  
674 *Geology*, 15(9-10), 1097-1121, [https://doi.org/10.1016/0191-8141\(93\)90158-7](https://doi.org/10.1016/0191-8141(93)90158-7), 1993.

675 Steinberger, B. and Calderwood, A.: Models of large-scale viscous flow in the Earth's mantle with constraints from mineral  
676 physics and surface observations. *Geophys. J. Int.*, 167, 1461-1481, [https://doi.org/10.1111/j.1365-  
677 246X.2006.03131.x](https://doi.org/10.1111/j.1365-246X.2006.03131.x), 2006

678 Styles, E., Davies, D. R., and Goes, S.: Mapping spherical seismic into physical structure: Biases from 3-D phase-transition  
679 and thermal boundary-layer heterogeneity. *Geophys. J. Int.*, 184, 1371–1378. [https://doi.org/10.1111/j.1365-](https://doi.org/10.1111/j.1365-246X.2010.04914.x)  
680 [246X.2010.04914.x](https://doi.org/10.1111/j.1365-246X.2010.04914.x), 2011.

681 Sturgeon W., Ferreira, A.M.G., Faccenda, M., Chang, S.-J. and Schardong, L.: On the origin of radial anisotropy near  
682 subducted slabs in the midmantle. *Geochem. Geophys. Geosys.* 20 (11), 5105-5125,  
683 <https://doi.org/10.1029/2019GC008462>, 2019.

684 Tape, W., and Tape, C. A reformulation of the Browaeys and Chevrot decomposition of elastic maps. *J. Elasticity.*  
685 <https://doi.org/10.1007/s10659-024-10056-x>, 2024.

686 Tasaka, M., Zimmerman, M. E., Kohlstedt, D. L., Stünitz, H. and Heilbronner, R. Rheological weakening of  
687 olivine + orthopyroxene aggregates due to phase mixing: Part 2. Microstructural development. *Journal Geophysical*  
688 *Research: Solid Earth*, 122, 7597–7612. <https://doi.org/10.1002/2017JB014311>, 2017.

689 Tommasi, A., Knoll, M., Vauchez, A., Signorelli, J. W., Thoraval, C. and Logé, R.: Structural reactivation in plate tectonics  
690 controlled by olivine crystal anisotropy. *Nature Geosci.*, 2, 423–427, <https://doi.org/10.1038/ngeo528>, 2009.

691 VanderBeek, B.P., Faccenda, M.: Imaging upper mantle anisotropy with teleseismic P-wave delays: insights from tomographic  
692 reconstructions of subduction simulations. *Geophys. J. Int.* 225, 2097–2119, 2021.

693 VanderBeek, B.P., Lo Bue, R., Rappisi, F. and Faccenda, M.: Imaging upper mantle anisotropy with travel-time and splitting  
694 intensity observations from teleseismic shear waves: Insights from tomographic reconstructions of subduction  
695 simulations. <https://doi.org/10.1093/gji/ggad389>, 2023.

696 Warren, J. M., Hirth, G. and Kelemen, P.B. Evolution of olivine preferred orientation during simple shear in the mantle. *Earth*  
697 *Planet. Sci. Lett.* 272, 501-512, <https://doi.org/10.1016/j.epsl.2008.03.063>, 2008.

698 Wookey, J. Direct probabilistic inversion of shear wave data for seismic anisotropy. *Geophys. J. Int.* 189, 1025-1037,  
699 <https://doi.org/10.1111/j.1365-246X.2012.05405.x>, 2012.

700 Zhou, Q., Hu, J., Liu, L., Chaparro, T., Stegman, D. R. and Faccenda, M.: Western U.S. seismic anisotropy revealing complex  
701 mantle dynamics. *Earth and Planet. Sci. Lett.* 500, 156-167, <https://doi.org/10.1016/j.epsl.2018.08.015>, 2018.

702  
703  
704  
705  
706  
707  
708  
709  
710  
711



712 **Appendix A. D-REX model vs analytical solution**

713 We compare the numerical solution of the D-REX model included in D-REX\_S and D-REX\_M with the analytical solution  
 714 provided by Fraters and Billen (2021, Supplementary Information) for a test with an upper mantle aggregate (*Ol:Ens* =  
 715 50:50) composed by 5 crystals for each phase,  $M^* = 50$ ,  $\chi = 0.3$ , and  $nCRSS = (1, 2, 3, \infty)$  for the four olivine slip systems  
 716  $[100](010)$ ,  $[100](001)$ ,  $[001](010)$ ,  $[001](100)$  (Table A1). For the first crystal, the time derivative of the cosine direction  
 717 matrix (CDM)  $\frac{\delta a_{ij}^v}{\delta t} = 0$  and the vorticity matrix  $\bar{\omega}_{ij}^v = \varepsilon_{jki}\omega_k^v = 0$ , while for the other 4 crystals:

$$719 \quad \frac{\delta a_{ij}^v}{\delta t} = \begin{bmatrix} -0.0040153 & -0.0010038 & 0.0020076 \\ -0.0085325 & -0.0010038 & 0.0065249 \\ -0.0130497 & -0.0010038 & 0.0110421 \end{bmatrix} \quad (A1)$$

720  
 721 with a maximum error of  $3.1 \cdot 10^{-3}$  % which we attribute to truncation errors, and:

$$723 \quad \bar{\omega}_{ij}^v = \begin{bmatrix} 0 & 0.005019 & 0.010038 \\ -0.005019 & 0 & 0.005019 \\ -0.010038 & -0.005019 & 0 \end{bmatrix} \quad (A2)$$

724  
 725 The changes in volume fractions are  $\frac{\delta f_m^v}{\delta t} = 0.630116863029$  for grain 1, and  $\frac{\delta f_m^v}{\delta t} = -0.157529215757$  for the other 4  
 726 crystals, resulting in a misfit of  $6.5244 \cdot 10^{-4}$  % relative to the analytical solution.

727 We provide the D-REX\_S\_test program for reproducing this simple test in the Supplementary Material.

728  
 729  
 730 Table A1 – Available slip systems of abundant anisotropic mantle phases present in D-REX\_S and D-REX\_M.

Slip system [uvw](hkl)	Olivine	Enstatite	Wadsleyite	Bridmanite	Post-Perovskite	
$[100](010)$	*		*	*	*	731 732
$[100](001)$	*		*	*	*	733
$[100](011)$			*			734
$[100](021)$			*			735
$[010](100)$				*	*	736
$[010](001)$				*	*	737
$[001](100)$	*	*		*	*	738
$[001](010)$	*		*	*	*	739
$[001]\{\bar{1}10\}$				*	*	740
$\langle \bar{1}10 \rangle (001)$				*		741
$\langle 110 \rangle \{\bar{1}10\}$				*	*	
$\frac{1}{2} \langle 111 \rangle \{101\}$			*			

## Appendix B. Aggregate elastic stiffness tensor

At any P-T condition, the single crystal elastic moduli  $C_{ij}^m$  are (in Voigt notation):

$$C_{ij}^m(P, T) = C_{ij}^m(P_0, T_0) + \partial C_{ij}^m / \partial P \cdot \Delta P + 0.5 \cdot \partial^2 C_{ij}^m / \partial P^2 \cdot \Delta P^2 + \partial C_{ij}^m / \partial T \cdot \Delta T + \partial^2 C_{ij}^m / \partial P \partial T \cdot \Delta P \Delta T \quad (B1)$$

where the partial derivatives are listed in Table A2 and  $\Delta P$  and  $\Delta T$  are deviations from the room conditions ( $P_0 = 10^{-4} \text{ GPa}$ ,  $T_0 = 298 \text{ K}$ ; Mainprice, 2007). The compliance tensor is the inverse of the stiffness tensor, i.e.,  $\mathbf{S}^m = \mathbf{C}^{m-1}$ . These tensors can be rotated as:

$$C_{ijkl}^v = a_{ip} a_{jq} a_{kr} a_{ls} C_{pqrs}^m \quad (B2a)$$

$$S_{ijkl}^v = a_{ip} a_{jq} a_{kr} a_{ls} S_{pqrs}^m \quad (B2b)$$

where  $\mathbf{a}$  is the CDM defining the crystal orientation with respect to the external reference frame. The stiffness and compliance tensors of the crystal aggregate (i.e., rock) are then obtained by arithmetic averaging:

$$\mathbf{C}^r = \sum_{m=1}^M X_m \sum_{v=1}^N X_v \mathbf{C}^v \quad (B3a)$$

$$\mathbf{S}^r = \sum_{m=1}^M X_m \sum_{v=1}^N X_v \mathbf{S}^v \quad (B3b)$$

where  $M = 2$  is the number of minerals in the two-phase mantle aggregates modelled in D-REX\_M and D-REX\_S,  $X_m$  their relative abundance,  $N$  the number of crystals of each phase,  $X_v$  the normalized crystal volume fraction ( $\sum_{v=1}^N X_v = 1$ ).  $\mathbf{C}^r$  and  $(\mathbf{S}^r)^{-1}$  correspond to the Voigt and Reuss average stiffness tensor of the rock, i.e.,  $\mathbf{C}_{Voigt}^r$  and  $\mathbf{C}_{Reuss}^r$ . More in general, the average stiffness tensor resulting from the linear combination of the two end-members is found as:

$$\bar{\mathbf{C}}^r = X_{Voigt} \mathbf{C}_{Voigt}^r + (1 - X_{Voigt}) \mathbf{C}_{Reuss}^r \quad (B4)$$

where  $X_{Voigt}$  is a free parameter defining the fraction of  $\mathbf{C}_{Voigt}^r$  relative to  $\mathbf{C}_{Reuss}^r$ . It is clear that the Hill average stiffness tensor  $\mathbf{C}_{Hill}^r$  is obtained when  $X_{Voigt} = 0.5$ .

The isotropic component of the average stiffness tensor  $\bar{C}_{ISO}^r$  can be assembled as  $\bar{C}_{ISO\_11}^r = \bar{C}_{ISO\_22}^r = \bar{C}_{ISO\_33}^r = K + \frac{4}{3}G$ ,  $\bar{C}_{ISO\_12}^r = \bar{C}_{ISO\_13}^r = \bar{C}_{ISO\_23}^r = K - \frac{2}{3}G$ ,  $\bar{C}_{ISO\_44}^r = \bar{C}_{ISO\_55}^r = \bar{C}_{ISO\_66}^r = G$ , knowing that:

$$K = \frac{[(\bar{C}_{11}^r + \bar{C}_{22}^r + \bar{C}_{33}^r) + 2(\bar{C}_{12}^r + \bar{C}_{13}^r + \bar{C}_{23}^r)]}{9} \quad (B5a)$$

$$G = \frac{[(\bar{C}_{11}^r + \bar{C}_{22}^r + \bar{C}_{33}^r) - (\bar{C}_{12}^r + \bar{C}_{13}^r + \bar{C}_{23}^r) + 3(\bar{C}_{44}^r + \bar{C}_{55}^r + \bar{C}_{66}^r)]}{15} \quad (B5b)$$

The isotropic component of the aggregate stiffness tensor  $\bar{C}_{ISO}^r$  is then replaced with the isotropic stiffness tensor  $C_{ISO}^{MMA\_EoS}$  obtained using the bulk and shear moduli from the lookup tables computed with the MMA\_EoS software (Chust et al., 2017) as:

$$\bar{C}_{MMA\_EoS}^r = \bar{C}^r + C_{ISO}^{MMA\_EoS} - \bar{C}_{ISO}^r \quad (B6)$$

Table B1: Composition (in mol%) used in MMA\_EoS to compute lookup tables for different mantle and basalt composition.

Lithology	Index	SiO <sub>2</sub>	MgO	FeO	CaO	Al <sub>2</sub> O <sub>3</sub>	Na <sub>2</sub> O	Source <sup>†</sup>
Dunite	1	40.43	42.45	16.07	0.51	0.51	0.04	(1)
Harzburgite	2	36.54	56.17	5.71	0.99	0.59	0.00	(2)
Pyrolite	3	38.71	49.85	6.17	2.94	2.22	0.11	(3)
Basalt	4	51.76	15.11	6.59	14.39	10.39	1.76	(2)
Pyroxenite	5	46.46	16.99	7.95	11.70	15.48	1.43	(4)

<sup>†</sup> (1) Kelemen and Ghiorso, 1986; (2) Chemia et al., 2015; (3) Workman and Hart, 2005; (4) Hirschmann et al., 2003.

795 Table B2 - Elastic moduli (GPa) and their P–T derivatives of the mineral phases present in ECOMAN. Temperature derivatives  
 796 are scaled by  $10^2$  GPa  $K^{-1}$ , and cross derivatives by  $10^{-3} K^{-1}$ .

Mineral	Index	Moduli	C11	C22	C33	C12	C13	C23	C44	C55	C66	Source <sup>†</sup>
Olivine	1	$M$	320.71	197.25	234.32	69.84	71.22	74.80	63.77	77.67	78.36	(1)
		$\partial M/\partial P$	5.41	5.26	3.78	1.88	1.53	1.60	1.08	1.42	1.80	(2)
		$\partial M/\partial T$	-4.02	-3.10	-3.53	-1.14	-0.96	-0.72	-1.26	-1.30	-1.56	(1)
Enstatite	2	$M$	236.90	180.50	230.40	79.60	63.20	56.80	84.30	79.40	80.10	(3)
		$\partial M/\partial P$	10.27	8.87	11.7	6.22	6.63	7.26	1.23	0.75	2.78	(3)
		$\partial^2 M/\partial P^2$	-0.47	-0.38	-0.53	-0.33	-0.26	-0.31	0	0	0	(3)
		$\partial M/\partial T$	-3.64	-3.43	-5.70	-1.52	-2.29	-1.63	-1.23	-1.58	-1.51	(4)
Wadsleyite	3	$M$	370.50	367.70	272.40	65.60	95.20	105.10	111.20	122.50	103.10	(5)
		$\partial M/\partial P$	5.21	6.83	8.06	4.06	3.30	3.30	1.39	0.00	1.88	(5)
		$\partial M/\partial T$	-4.02	-3.10	-3.53	-1.14	-0.96	-0.72	-1.26	-1.30	-1.56	(1)
Wadsleyite Fe = 0.94 H2O = 0.15 wt%	4	$M$	341.00	358.00	224.00	75.00	99.00	102.00	106.00	109.00	90.80	(6)
		$\partial M/\partial P$	7.80	5.37	10.5	4.60	2.33	4.20	0.87	0.84	2.43	(6)
		$\partial^2 M/\partial P^2$	-0.26	0	-0.46	-0.11	0	-0.14	0	0	-0.053	(6)
		$\partial M/\partial T$	-2.90	-3.60	-4.00	-0.60	-1.90	-1.20	-1.80	-1.10	-1.30	(6)
Ringwoodite	5	$M$	329.00	-	-	118.00	-	-	130.00	-	-	(7)
		$\partial M/\partial P$	6.20	-	-	0.80	-	-	2.80	-	-	(7)
		$\partial M/\partial T$	-4.90	-	-	-0.70	-	-	-1.30	-	-	(7)
Garnet	6	$M$	299.10	-	-	106.70	-	-	93.70	-	-	(8)
		$\partial M/\partial P$	6.54	-	-	2.87	-	-	1.72	-	-	(8)
		$\partial M/\partial T$	-3.05	-	-	-0.58	-	-	-0.71	-	-	(9)
Bridgmanite	7	$M$	484.00	542.00	477.00	146.00	146.00	162.00	195.00	172.00	151.00	(9)
		$\partial M/\partial P$	3.40	5.30	5.20	3.30	2.40	2.50	1.40	0.80	1.40	(10)
		$\partial M/\partial T$	-1.80	-3.30	-2.20	-0.40	-0.20	-0.50	-2.20	-0.60	-1.60	(10)
		$\partial^2 M/\partial P\partial T$	-0.017	-0.016	-0.016	-0.006	-0.006	-0.007	-0.0005	-0.0005	-0.004	(10)
Bridgmanite P0 = 34 GPa T0 = 1500 K	8	$M$	581.42	669.06	626.31	249.02	212.93	239.01	228.63	220.26	183.89	(11)
		$\partial M/\partial P$	3.73	5.54	5.47	3.30	2.48	2.53	1.38	0.85	1.56	(11)
		$\partial M/\partial T$	-3.99	-5.53	-4.32	-1.76	-0.64	-0.26	-2.12	-1.25	-1.96	(11)
		$\partial^2 M/\partial P\partial T$	-0.16	-0.044	-0.051	-0.017	-0.06	-0.035	-0.017	-0.044	-0.042	(10)
Bridgmanite P0 = 48 GPa T0 = 1500 K	9	$M$	601.83	698.17	652.27	271.81	236.00	265.58	233.53	205.41	190.43	(11)
		$\partial M/\partial P$	3.73	5.54	5.47	3.30	2.48	2.53	1.38	0.85	1.56	(11)
		$\partial M/\partial T$	-3.14	-5.94	-4.53	-1.94	-0.55	-0.59	-2.15	-1.26	-2.50	(11)
		$\partial^2 M/\partial P\partial T$	-0.66	-0.026	-0.034	-0.158	-0.008	-0.160	-0.001	-0.036	-0.002	(11)
Ferropiclasite	10	$M$	300.0	-	-	93.60	-	-	147.0	-	-	(12)
		$\partial M/\partial P$	9.56	-	-	1.45	-	-	1.03	-	-	(12)
		$\partial M/\partial T$	-5.98	-	-	0.89	-	-	-0.88	-	-	(12)
		$\partial^2 M/\partial P\partial T$	0.56	-	-	0.06	-	-	0.20	-	-	(12)
post-Perovskite P0 = 99.95 GPa T0 = 1500 K	11	$M$	1124.75	884.22	1124.32	350.69	287.53	461.05	254.57	231.19	344.05	(13)
		$\partial M/\partial P$	5.85	2.70	5.44	3.06	3.00	2.33	1.37	1.27	2.06	(13)
		$\partial M/\partial T$	1.01	-5.24	-4.90	-0.92	-0.51	-1.78	-0.81	-2.33	-2.19	(13)
		$\partial^2 M/\partial P\partial T$	-0.937	0.709	0.797	0.60	-0.801	0.692	-0.107	-0.186	-0.16	(13)

797 <sup>†</sup> (1) Isaak, 1992; (2) Zha et al., 1998; (3) Chai et al., 1992; (4) Jackson et al., 2007; (5) Zha et al., 1997; (6) Zhou et al.,  
 798 2022; (7) Sinogeikin et al., 2003; (8) Chai and Brown, 1997; (9) Sinogeikin and Bass, 2002; (10) Wentzcovitch et al.,  
 799 2004. Derivatives at (100 GPa, 300 K); (11) Zhang et al., 2013. Derivatives extrapolated by interpolation; (12) Karki  
 800 et al., 2000; (13) Zhang et al., 2016. Derivatives extrapolated by interpolation.

803 **Appendix C. Velocity gradient tensor in polar coordinates**

804 In polar grids the velocity field is typically defined by the longitudinal, radial and, in 3D, colatitudinal components  $\vec{V}_{(\phi,r,\theta)} =$   
 805  $(V_\phi, V_r, V_\theta)$ . However, the crystals' orientation and their rotation are defined relative to the external Cartesian reference frame.  
 806 As such, the velocity gradient tensor must be computed in Cartesian coordinate system. This is done by rotating the velocity  
 807 field from spherical to Cartesian coordinates as:

$$808 \quad \begin{bmatrix} V_x \\ V_y \\ V_z \end{bmatrix} = \begin{bmatrix} -\sin\phi & \sin\theta\cos\phi & \cos\theta\cos\phi \\ \cos\phi & \sin\theta\sin\phi & \cos\theta\sin\phi \\ 0 & \cos\theta & -\sin\theta \end{bmatrix} \begin{bmatrix} V_\phi \\ V_r \\ V_\theta \end{bmatrix} \quad (C1)$$

810  
 811 Using the finite difference approach, the spatial gradients of the Cartesian velocity components are computed on the spherical  
 812 grid as:

$$813 \quad \mathbf{L}_{\substack{(x,y,z) \\ (\phi,r,\theta)}} = \frac{\partial \vec{V}_{(x,y,z)}}{\partial(\phi, r, \theta)} = \begin{bmatrix} \frac{\partial V_x}{\partial \phi} & \frac{\partial V_x}{\partial r} & \frac{\partial V_x}{\partial \theta} \\ \frac{\partial V_y}{\partial \phi} & \frac{\partial V_y}{\partial r} & \frac{\partial V_y}{\partial \theta} \\ \frac{\partial V_z}{\partial \phi} & \frac{\partial V_z}{\partial r} & \frac{\partial V_z}{\partial \theta} \end{bmatrix} \quad (C2)$$

814  
 815  
 816 Defining  $\mathbf{J}$  as the Jacobian matrix:

$$817 \quad \mathbf{J} = \frac{\partial(\phi, r, \theta)}{\partial(x, y, z)} = \begin{bmatrix} \frac{\partial \phi}{\partial x} & \frac{\partial \phi}{\partial y} & \frac{\partial \phi}{\partial z} \\ \frac{\partial r}{\partial x} & \frac{\partial r}{\partial y} & \frac{\partial r}{\partial z} \\ \frac{\partial \theta}{\partial x} & \frac{\partial \theta}{\partial y} & \frac{\partial \theta}{\partial z} \end{bmatrix} = \begin{bmatrix} -\sin\phi/(r \cdot \sin\theta) & \cos\phi/(r \cdot \sin\theta) & 0 \\ \sin\theta\cos\phi & \sin\theta\sin\phi & \cos\theta \\ \cos\theta\cos\phi/r & \cos\theta\sin\phi/r & -\sin\theta/r \end{bmatrix} \quad (C3)$$

818  
 819  
 820 the velocity gradient tensor in Cartesian coordinates is  $\mathbf{L}_{\substack{(x,y,z) \\ (x,y,z)}} = \mathbf{L}_{\substack{(x,y,z) \\ (\phi,r,\theta)}} \mathbf{J}$ :

$$821 \quad \mathbf{L}_{\substack{(x,y,z) \\ (x,y,z)}} = \frac{\partial \vec{V}_{(x,y,z)}}{\partial(x, y, z)} = \begin{bmatrix} \frac{\partial V_x}{\partial x} & \frac{\partial V_x}{\partial y} & \frac{\partial V_x}{\partial z} \\ \frac{\partial V_y}{\partial x} & \frac{\partial V_y}{\partial y} & \frac{\partial V_y}{\partial z} \\ \frac{\partial V_z}{\partial x} & \frac{\partial V_z}{\partial y} & \frac{\partial V_z}{\partial z} \end{bmatrix} = \begin{bmatrix} \frac{\partial V_x}{\partial \phi} & \frac{\partial V_x}{\partial r} & \frac{\partial V_x}{\partial \theta} \\ \frac{\partial V_y}{\partial \phi} & \frac{\partial V_y}{\partial r} & \frac{\partial V_y}{\partial \theta} \\ \frac{\partial V_z}{\partial \phi} & \frac{\partial V_z}{\partial r} & \frac{\partial V_z}{\partial \theta} \end{bmatrix} \begin{bmatrix} \frac{\partial \phi}{\partial x} & \frac{\partial \phi}{\partial y} & \frac{\partial \phi}{\partial z} \\ \frac{\partial r}{\partial x} & \frac{\partial r}{\partial y} & \frac{\partial r}{\partial z} \\ \frac{\partial \theta}{\partial x} & \frac{\partial \theta}{\partial y} & \frac{\partial \theta}{\partial z} \end{bmatrix} \quad (C4)$$

## 824 **Appendix D. Aggregate rotation due to fluid body rotation**

825 When multiple creep mechanisms are active, we assume that only the fraction of deformation accommodated by dislocation  
 826 creep contributes to the LPO development. This fraction of the total deformation is defined as  $F_d = \eta_{eff}/\eta_{disl}$ , where  
 827  $0 \leq F_d \leq 1$  is interpolated from the large-scale geodynamic model,  $\eta_{eff}$  is the effective viscosity resulting from the harmonic  
 828 average of the viscosities from the flow law of different creep mechanisms,  $\eta_{disl}$  the viscosity from the dislocation creep flow  
 829 law. At a given timestep  $\Delta t$ , crystal rotation according to the D-REX model is applied for the fraction  $\Delta t_{disl} = \Delta t \cdot F_d$ , while  
 830 for the remaining time  $\Delta t_{diff} = \Delta t \cdot (1 - F_d)$  we follow the numerical study of Hedjazian et al. (2017) and apply fluid body  
 831 rotation by multiplying the CDM of the aggregates with the rotation of the FSE. In this way, we preserve and do not alter the  
 832 strength of the LPO.

833 Given the orthogonal CDMs defining the original and final crystal orientation  $\mathbf{a}^t$  and  $\mathbf{a}^{t+\Delta t_{diff}}$ , and those defining the original  
 834 and final FSE semiaxes orientation  $\mathbf{v}^t$  and  $\mathbf{v}^{t+\Delta t_{diff}}$  (i.e., the eigenvectors of, respectively, the left stretch tensor  $\mathbf{LS}^t =$   
 835  $\mathbf{F}^t(\mathbf{F}^t)^T$  and  $\mathbf{LS}^{t+\Delta t_{diff}} = \mathbf{F}^{t+\Delta t_{diff}}(\mathbf{F}^{t+\Delta t_{diff}})^T$ ), the following relation implies that after fluid body rotation the orientation  
 836 of the crystal relative to FSE semiaxes must remain constant:

$$837 \mathbf{a}^{t+\Delta t_{diff}} \mathbf{v}^{t+\Delta t_{diff}} = \mathbf{a}^t \mathbf{v}^t \quad (D1)$$

839  
 840 The new crystal orientation is then:

$$841 \mathbf{a}^{t+\Delta t_{diff}} = \mathbf{a}^t \mathbf{v}^t (\mathbf{v}^{t+\Delta t_{diff}})^{-1} = \mathbf{a}^t \mathbf{v}^t (\mathbf{v}^{t+\Delta t_{diff}})^T \quad (D2)$$

842  
 843  
 844

## 845 **Additional References**

- 846 M. Chai and J. Brown. The elastic constants of a pyrope-grossular-almandine garnet to 20 GPa. *Geophys. Res. Lett.*,  
 847 24(5):523–526, 1997.
- 848 M. Chai, J. Brown, and L. Slutski. The elastic constants of an aluminous orthopyroxene to 12.5 GPa. *J. Geophys. Res.*,  
 849 102(14):779–785, 1992.
- 850 Z. Chemia, D. Dolejš, and G. Steinle-Neumann. Thermal effects of variable material properties and metamorphic reactions in  
 851 a three-component subducting slab. *J. Geo-phys. Res.*, 120:6823–6845, 2015.
- 852 M. Hirschmann, T. Kogiso, M. Baker, and E. Stopler. Alkalic magmas generated by partial melting of garnet pyroxenite.  
 853 *Geology*, 31:481–484, 2003.
- 854 D. Isaak. High-temperature elasticity of iron-bearing olivines. *J. Geophys. Res.*, 97: 1871–1885, 1992.
- 855 J. Jackson, S. Sinogeikin, and J. Bass. Sound velocities and single-crystal elasticity of orthoenstatite to 1073 K at ambient  
 856 pressure. *Phys. Earth Planet. Int.*, 171:1–12, 2007.

- 857 B. Karki, R. Wentzcovitch, S. de Gironcoli, and S. Baroni. High-pressure lattice dynamics and thermoelasticity of MgO. *Phys.*  
858 *Rev. B*, 61:8793–8800, 2000.
- 859 P. Kelemen and M. Ghiorso. Assimilation of peridotite in zoned calc-alkaline plutonic complexes: evidence from the big jim  
860 complex, Washington Cascades. *Contrib. Min.*, 94:12–28, 1986.
- 861 David Mainprice. Seismic Anisotropy of the Deep Earth from a Mineral and Rock Physics Perspective. *Treatise on Geophysics*,  
862 2, Editor: G. Schubert, Elsevier, pp.437-491, 2007.
- 863 S. Sinogeikin and J. Bass. Elasticity of pyrope and majorite – pyrope solid solutions to high temperatures. *Earth Planet. Sci.*  
864 *Lett.*, 203:549–555, 2002.
- 865 S. Sinogeikin, J. Bass, and K. Katsura. Single-crystal elasticity of ringwoodite to high pressures and high temperatures:  
866 implications for 520 km seismic discontinuity. *Phys. Earth Planet. Int.*, 136:41–66, 2003.
- 867 R. Wentzcovitch, B. Karki, M. Cococcioni, and S. de Gironcoli. Properties of MgSiO<sub>3</sub>-perovskite: Insights on the nature of  
868 the earth’s lower mantle. *Phys. Rev. Lett.*, 92, 2004.
- 869 R. Workman and S. Hart. Major and trace element composition of the depleted morb mantle. *Earth Planet. Sci. Lett.*, 231:53–  
870 72, 2005.
- 871 C. Zha, T. Duffy, H. Mao, R. Downs, R. Hemley, and D. Weidner. Single-crystal elasticity of  $\beta$ -Mg<sub>2</sub>SiO<sub>4</sub>, to the pressure of  
872 the 410 km seismic discontinuity in the earth’s mantle. *Earth Planet. Sci. Lett.*, 147:E9–E15, 1997.
- 873 C. Zha, T. Duffy, R. Downs, H. Mao, and R. Hemley. Brillouin scattering and x-ray diffraction of San Carlos olivine: direct  
874 pressure determination to 32 GPa. *Earth Planet. Sci. Lett.*, 159:25–33, 1998.
- 875 Z. Zhang, L. Stixrude, and J. Brodholt. Elastic properties of MgSiO<sub>3</sub>-perovskite under lower mantle conditions and the  
876 composition of the deep earth. *Earth Planet. Sci. Lett.*, 379:1–12, 2013.
- 877 Z. Zhang, S. Cottaar, L. Tao, S. Stackhouse, and B. Militzer. High-pressure, temperature elasticity of Fe- and Al-bearing  
878 MgSiO<sub>3</sub>: Implications for the earth’s lower mantle. *Earth Planet. Sci. Lett.*, 434:264–273, 2016.
- 879 W.-Y. Zhou, M. Hao, J. Zhang, B. Chen, R. Wang, and B. Schamndt. Constraining composition and temperature variations in  
880 the mantle transition zone. *Nat. Comm.*, 13:1094, doi: 10.1038/s41467-022-28709-7, 2022.